ADVANCING EARTH AND SPACE SCIENCE

JGR Solid Earth

RESEARCH ARTICLE
10.1029/2022JB024059

3D Coseismic Surface Displacements From Historical Aerial Photographs of the 1987 Edgecumbe Earthquake, New Zealand

J. E. Delano[1], A. Howell[1,2], T. A. Stahl[1], and K. Clark[2]

[1]School of Earth and Environment, University of Canterbury, Christchurch, New Zealand, [2]GNS Science, Lower Hutt, New Zealand

Key Points:

- Historical aerial photos can be used to generate pre- and post-earthquake digital surface models for measuring displacement
- This method performs at least as well as field surveys, and better captures single-event displacements to constrain earthquake behavior
- The Edgecumbe earthquake is important for understanding low dip-angle normal fault ruptures and possibly magma-tectonic interactions

Correspondence to:

J. E. Delano,
jaimedelano@gmail.com

Citation:

Delano, J. E., Howell, A., Stahl, T. A., & Clark, K. (2022). 3D coseismic surface displacements from historical aerial photographs of the 1987 Edgecumbe earthquake, New Zealand. *Journal of Geophysical Research: Solid Earth*, *127*, e2022JB024059. https://doi.org/10.1029/2022JB024059

Received 17 JAN 2022
Accepted 29 OCT 2022

Author Contributions:

Conceptualization: J. E. Delano, A. Howell, T. A. Stahl, K. Clark
Formal analysis: J. E. Delano
Funding acquisition: T. A. Stahl, K. Clark
Investigation: J. E. Delano
Methodology: J. E. Delano, A. Howell, T. A. Stahl
Resources: T. A. Stahl, K. Clark
Software: A. Howell
Supervision: A. Howell, T. A. Stahl, K. Clark
Validation: A. Howell, T. A. Stahl
Visualization: J. E. Delano
Writing – original draft: J. E. Delano
Writing – review & editing: J. E. Delano, A. Howell, T. A. Stahl, K. Clark

Abstract Earthquake surface deformation provides key constraints on the geometry, kinematics, and displacements of fault rupture. However, deriving these characteristics from past earthquakes is complicated by insufficient knowledge of the pre-event landscape and its post-event modification. The 1987 M_w 6.5 Edgecumbe earthquake in the northern Taupō volcanic zone (TVZ) in New Zealand represents a moderate-magnitude earthquake with distributed surface rupture that occurred before widespread high-resolution topographic data were available. We use historical aerial photos to build pre- and post-earthquake digital surface models (DSMs) using structure-from-motion techniques. We measured discrete and distributed deformation from differenced DSMs and compared the effectiveness of the technique to traditional field- and lidar-based studies. We identified most fault traces recognized by 1987 field mapping, mapped newly identified traces, and made dense remote slip measurements with a vertical separation resolution of ~0.3 m. Our maximum and average vertical separation measurements on the Edgecumbe fault trace (2.5 ± 0.3 and 1.2 m, respectively), are similar to field-based values of 2.4 and 1.1 m, respectively. Importantly, this technique can discern between new and pre-existing fault scarps better than field techniques or post-earthquake lidar-based measurements alone. Our surface displacement results are used to refine subsurface fault geometries and slip distributions at depth, which are further used to investigate potential magmatic-tectonic stress interactions in the northern TVZ. Our results suggest the Edgecumbe fault dips more gently at depth than at the surface, hosted shallow slip in 1987, and may be advanced toward failure by interactions with nearby magma bodies.

Plain Language Summary Understanding earthquake behavior relies heavily on information about how past earthquakes changed the landscape. Detailed information about the surface topography before the earthquake is often limited, creating challenges for accurately measuring earthquake surface deformation. Aerial photos are widely available and can be used to create 3D digital surface models in places where other topographic information is lacking. We use historical aerial photos to make 3D datasets of the surface topography before and after the 1987 Edgecumbe earthquake in New Zealand. We calculated the difference between the two 3D datasets to identify and measure how the earthquake changed the landscape, and compared our results to previous measurements. We found that this method generally works as well as field methods for identifying and measuring fault movement, and has some advantages over other techniques. In particular, this approach can separate deformation from individual earthquakes, which had previously been a challenge. The results refine our understanding of the faults below the surface, provide insight into the earthquake's relationship to surrounding faults and volcanic systems, and allow us to better characterize seismic hazard both here and in other similar geologic settings.

1. Introduction

Historical earthquakes provide one of the best opportunities to characterize surface ruptures and the hazards posed by coseismic deformation (e.g., Wesnousky, 2008; Youngs et al., 2003). Empirical scaling laws and fault displacement hazard analyses are largely based on inventories of surface-deforming events that have occurred over the last ~150 years. However, accurately deriving surface rupture and displacement characteristics from historical earthquakes can be challenging, particularly for events that occurred before satellite- and lidar-based datasets became widely available. In regions with infrequent earthquakes, high-relief scarps, and/or low erosion rates, modern high-resolution topographic data can capture many characteristics of older historical earthquake ruptures (e.g., DuRoss et al., 2019; Middleton et al., 2016; Nissen et al., 2014; Shao et al., 2020). Elsewhere, reconnaissance

10.1029/2022JB024059

mapping (if undertaken at the time) or sparse paleoseismic trenches may be the only records of historical ruptures (e.g., Ambraseys, 1963; Henderson, 1933; Kelsey et al., 1998; Schermer et al., 2004). The details of coseismic deformation in these dynamic landscapes may be lost over time to erosion, vegetation growth, or anthropogenic modification. For many historical earthquakes, assumptions about pre-earthquake topography and landscape modification between the timing of the event and data collection add significant uncertainties to reconstructions of displacements and rupture extent.

Historical and modern aerial photographs occupy a useful niche for studying earthquakes because they span long periods of time (70+ years), often with repeat surveys. With more recent advances in photogrammetry techniques, existing aerial photographs can be used to generate additional pre- and post-earthquake topographic data to supplement lidar, satellite, and field-based data (e.g., Andreuttiova et al., 2022; Howell et al., 2020; Zhou et al., 2016). This means that high-resolution 2D and 3D displacement fields, typically only achievable for recent ruptures with modern techniques like differential lidar or InSAR, can theoretically be produced for any earthquake where sufficient-quality pre- and post-event photos are available. Surface displacements derived from aerial imagery can serve as a compromise between resolution, coverage, and availability compared to other remote sensing or field data.

Legacy aerial images (i.e., collected from airplane-based surveys) have some advantages over other remote sensing techniques and can be applied over a variety of geologic settings. Post-earthquake field surveys, including fault rupture mapping, offset measurements, and unmanned aerial vehicle (UAV) surveys can capture fine-scale and ephemeral features (e.g., Beanland et al., 1989; Blick & Flaherty, 1989; DuRoss et al., 2019; Koehler et al., 2021; Litchfield et al., 2018; Trexler et al., 2018). However, these surveys may miss subtle, broader-scale deformation, can be hindered by time, weather, and access, or have uncertainties that are difficult to quantify. Low-altitude UAV photosets have the resolution for measuring coseismic displacements and even interseismic creep (e.g., Scott et al., 2020), but are limited to the last decade and are typically purpose-collected after an event. Aerial and terrestrial lidar data across earthquake ruptures provide high-resolution, geometrically accurate data in 3D (e.g., Duffy et al., 2013; Oskin et al., 2012; Wedmore et al., 2019) and the bare-earth capabilities outperform image-based methods in vegetated areas (Ekhtari & Glennie, 2018). Lidar data, however, is expensive to collect and typically requires reconnaissance to define the area of interest, so coverage over the full deformation field may be incomplete, such as for the 2016 Kaikōura earthquake (e.g., Litchfield et al., 2018). With any survey method, pre-earthquake topography is commonly unavailable so is often inferred or gathered from other sources (e.g., Lajoie et al., 2020). Satellite-based data (InSAR and satellite images) have the advantage of frequent data collection, but are limited to the last few decades. Satellite imagery resolution may be too coarse for smaller displacements, and InSAR suffers from data loss where strain is high near the fault trace (e.g., Elliott et al., 2016).

This study focuses on the 1987 Edgecumbe earthquake as an example of surface rupture that can be comprehensively reconstructed with pre- and post-earthquake aerial imagery, filling the gap between the historical event timing (1987) and lidar collection in 2006 and 2011. We use legacy aerial photos of the Rangitāiki Plains in the North Island of New Zealand (Figure 1) and photogrammetry software to generate pre- and post-earthquake digital surface models (DSMs) and orthophoto mosaics from the 1987 Edgecumbe earthquake. Most existing studies that use similar remote sensing techniques (i.e., historical airplane-based photos) focus on larger magnitude (M_w 7+) earthquakes where slip is more easily resolved (e.g., Barnhart et al., 2019; Howell et al., 2020; Zhou et al., 2016). The M_w 6.5 Edgecumbe earthquake, conversely, represents a moderate magnitude earthquake with <2 m average surface slip (Beanland et al., 1989), and therefore tests the limits of this technique with a final topographic product resolution that approaches the scale of surface displacement. The existence of several different displacement datasets (lidar, leveling surveys, and field measurements) allow for robust sensitivity tests of our method and provide realistic constraints on the limits of using historical aerial photographs to characterize coseismic deformation. We demonstrate the utility of the technique in elucidating tectonic-magmatic interactions, which is one of the fundamental processes regulating earthquake behavior in this back-arc rift setting (e.g., Muirhead et al., 2022; Rowland et al., 2010; Villamor & Berryman, 2001). The new surface deformation data were used to solve for the best-fitting slip and fault geometry and to forward model stress interactions with a magmatic sill at the base of the seismogenic crust. These new datasets provide a more complete picture of fault rupture hazards from moderate-magnitude normal-fault earthquakes as well as insights into possible interactions between magmatic and tectonic processes in the Taupō volcanic zone (TVZ) and elsewhere.

10.1029/2022JB024059

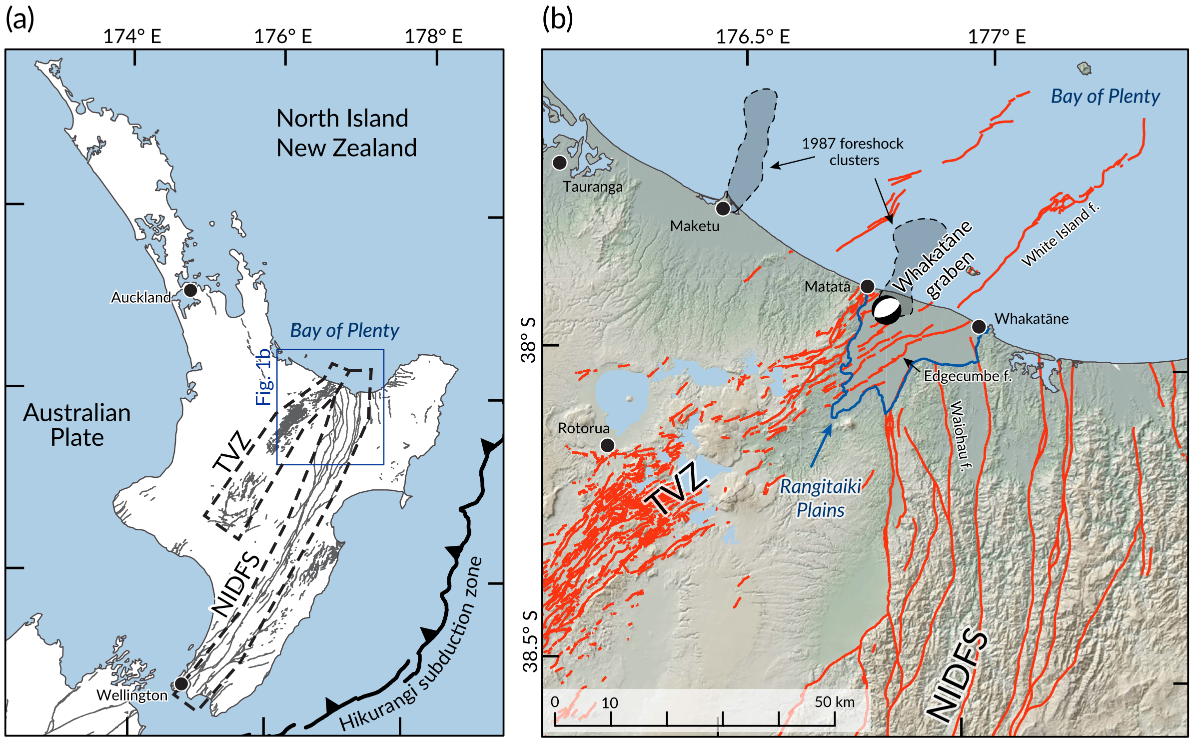

Figure 1. Tectonic setting of the 1987 Edgecumbe earthquake. (a) The Edgecumbe earthquake occurred in the northern Taupō volcanic zone (TVZ), a zone of backarc extension in the Australian plate above the Hikurangi subduction zone. Active onshore faults in gray (Langridge et al., 2016). (b) The Edgecumbe earthquake surface rupture occurred mostly within the Rangitāiki Plains– lowlands in the onshore Whakatāne graben at the intersection of the TVZ and North Island dextral fault system (NIDFS). Active faults shown in red. Onshore faults from Langridge et al. (2016). Only graben-bounding offshore faults are shown (Lamarche et al., 2006). Focal mechanism from Anderson and Webb (1989). Foreshock locations from Smith and Oppenheimer (1989).

2. Background

2.1. Geologic Setting

The 1987 Edgecumbe earthquake occurred within the Whakatāne graben at the northern end of the onshore Taupō rift on the North Island of New Zealand (Figure 1) (Beanland et al., 1989). The Taupō rift (or Taupō fault belt) is a region of localized normal faults in the TVZ, the continental volcanic arc associated with the Hikurangi subduction zone (Figure 1) (e.g., Wilson et al., 1995). GNSS data show the northernmost TVZ is extending at a rate of ∼15 mm/yr (Lamarche et al., 2006; Wallace et al., 2004).

The structure of the Whakatāne graben is primarily controlled by the northwest-dipping Edgecumbe-White Island fault; the White Island fault is the offshore continuation of the onshore Edgecumbe fault (Figure 1b) (Lamarche et al., 2006). The Edgecumbe fault accommodates primarily normal motion and displaces basement greywacke overlain by a succession of alluvial, wetland, and marine sediments, erupted rocks, and reworked volcanic deposits that make up the Rangitāiki Plains (Beanland et al., 1990; Ota et al., 1988). The eastern margin of the onshore Whakatāne graben is located within the Rangitāiki Plains and coincides with a transitional zone where the dominantly strike-slip North Island dextral fault system (also referred to as North Island dextral fault belt and North Island fault system) and the extensional Taupō Rift begin to intersect (Figure 1) (Mouslopoulou et al., 2008). The western margin of the onshore Whakatāne graben is thought to be largely controlled by the east-dipping Matatā fault (e.g., Begg & Mouslopoulou, 2010; Ota et al., 1988). Active volcanoes are located in the northeast (offshore) and southwest (onshore) sections of the graben, and off-axis magma chamber inflation has been inferred immediately west of Matatā (Hamling et al., 2016). Taken together, previous studies demonstrate that the Edgecumbe earthquake occurred in a relatively simple graben within a complex tectonic setting (e.g., Wilson & Rowland, 2016).

The M_w 6.5 Edgecumbe earthquake occurred on 2 March 1987 (local time) and produced widespread subsidence from normal slip (Anderson et al., 1990; Beanland et al., 1990; Darby, 1989; Webb & Anderson, 1998). Poor instrument distribution leads to some uncertainty in the rupture mechanism and locations of the hypocenter and centroid, but the most recent estimates indicate a relatively shallow centroid depth (6 ± 1 km) on a gently dipping fault plane (32° + 5/–10°) striking southwest (229 ± 10°) with dominantly normal rake (−113 ± 12°) (Figure 1b) (Webb & Anderson, 1998). Seismological studies interpreted that the mainshock initiated near the northern, lower edge of the Edgecumbe fault and the rupture propagated unilaterally toward the southwest (Anderson & Webb, 1989; Webb & Anderson, 1998).

The mainshock was preceded by foreshocks (starting 21 February 1987) in two southwest-trending clusters: one in the Whakatāne graben between Matatā and Thornton and the other farther northwest near Maketu (Figure 1b) (Smith & Oppenheimer, 1989). The Edgecumbe earthquake aftershocks were primarily between 4 and 6 km depth and were nearly all <8 km deep, which together indicate a brittle ductile boundary at 6–8 km depth near the Rangitāiki Plains (Robinson, 1989).

The 1987 Edgecumbe earthquake ruptured a number of pre-existing, but previously unrecognized faults in the onshore Whakatāne graben (Beanland et al., 1989). Following earthquake, field-based surveys conducted fault trace mapping, discrete horizontal and vertical displacement measurements along surface ruptures, limited short (<50-m-long) topographic profile measurements, and leveling surveys along the major roads (Beanland et al., 1989; Blick & Flaherty, 1989). Most of the slip occurred on the Edgecumbe fault, the inferred primary structure on which the mainshock initiated (Beanland et al., 1989). The earthquake also produced many short surface ruptures on widely spaced faults up to 8 km away from the main trace. The field-based Edgecumbe fault measurements yielded a maximum normal dip slip of 3.1 m (2.5 m throw and 1.3 m heave) along a 7-km-long trace, with no evidence of strike-slip motion (Beanland et al., 1989). The surface slip was high compared to other recorded normal fault earthquakes (Beanland et al., 1990); globally derived displacement-length scaling relationships suggest that the average and maximum slip of the Edgecumbe earthquake are more consistent with fault ruptures 4–6.5x its mapped length (Wesnousky, 2008). Repeat road leveling surveys in the Rangitāiki plains identified no uplift within the Edgecumbe fault footwall and estimated that ∼10% of coseismic displacement values were accommodated as afterslip in the months following the earthquake. These leveling surveys, however, are limited to only a few roads, are complicated by sparse pre-earthquake survey reference data, lacked an absolute reference frame, likely includes non-tectonic deformation, and transect the main fault at an oblique angle outside the zone of peak slip (Blick & Flaherty, 1989) (Text S1).

2.2. Remote Slip Measurements From Historical Earthquakes

Earthquake surface deformation can be used to resolve fault geometry and kinematics, and fault slip measurements using airborne remote sensing (e.g., lidar and photogrammetric datasets) have been fundamental in understanding fault rupture behavior and seismic hazard (e.g., Manighetti et al., 2015, 2020; Perrin et al., 2016). Regularly-spaced fault displacement measurements provide insights into both single-event and long-term rupture segmentation (e.g., Manighetti et al., 2020); fault growth, maturity, possible rupture directivity (Perrin et al., 2016); and how faults accommodate elastic-inelastic strain (Barnhart et al., 2019; Scott et al., 2019). A number of techniques exist to measure single-event coseismic deformation and resolve slip from optical and lidar datasets, including 3D point cloud differencing (iterative closest point, or ICP, algorithm; after Nissen et al., 2012), pixel-tracking (e.g., Barnhart et al., 2020; Leprince et al., 2007; Milliner et al., 2015; Scott et al., 2018), and basic DSM differencing and manual feature-tracking for vertical and horizontal displacements, respectively. These multi-temporal data remove ambiguity in correlating cumulative displacements to individual earthquakes, which can be particularly important when characterizing off-fault deformation and the role of small-offset or secondary structures in the earthquake rupture process (Andreuttiova et al., 2022; Duffy et al., 2013; Oskin et al., 2012; Wedmore et al., 2019). Together with seismic observations, coseismic slip distributions can also reveal the influence of extrinsic (e.g., volcanic) processes on fault rupture (e.g., Scott et al., 2019; Yagi et al., 2016). While the number of multi-temporal studies increases with each additional surface rupturing earthquake, relatively few datasets currently exist, making historical case studies critically important in advancing earthquake science.

2.3. Capturing Coseismic Deformation Using Structure-From-Motion and Legacy Aerial Photos

Structure-from-motion (SfM) is a photogrammetry-based technique that takes 2D photos, shot from different locations or view angles, and creates 3D point clouds of the surface. The success of SfM-based topographic products is largely dependent on the photo set quality, coverage, and resolution. An ideal photoset for SfM techniques has detailed image resolution to produce accurate photo tie points (e.g., Westoby et al., 2012), ample (~60%) overlap between photos (Abdullah et al., 2013; Bakker & Lane, 2017; Krauss, 1993), an extent larger than the area of interest (e.g., Reitman et al., 2015), and is taken with the same camera and specifications with no changes in lighting or the subject (e.g., Bemis et al., 2014).

For aerial photos, the above SfM requirements translate to a photoset captured at a low flight altitude (resulting in high image detail resolution) with the same camera, lens, and settings. Assuming a constant flight speed, image overlap is a function of image capture rate and the lens focal length; longer focal lengths have a narrower view angle and thus less overlap between images for the same capture rate. Some photo sets comprise more than one flight that can include changes in lighting (different sun angle), vegetation cover (different seasons), and changes to the built or agricultural environment. Thus, the ideal pre- or post-event aerial photosets should minimize the number of flights and overall elapsed time as well as differences in sunlight and season to reduce changes and artifacts caused by non-tectonic processes.

In contrast to traditional photogrammetry, SfM methods rely on internal bundle adjustments and therefore can be used with legacy aerial photo sets without original camera, photo, and location metadata (e.g., Derrien et al., 2015; Gomez et al., 2015; Lajoie et al., 2020; Westoby et al., 2012). With film aerial photos in particular, however, SfM results generally improve when additional camera calibration, photo fiducial, and survey specifications are provided (e.g., Stahl et al., 2021). Some georeference data is also required, but can be extracted from freely available topographic datasets or modern geodetic surveys (e.g., Lajoie et al., 2020; Midgley & Tonkin, 2017).

Previous studies using legacy aerial photographs to characterize coseismic deformation are limited and primarily focus on 2D lateral displacements (e.g., Ayoub et al., 2009; Milliner et al., 2015). Vertical differencing and 3D displacement measurements are typically reserved for M_w 7+ earthquakes because the large surface displacements yield higher elevation signal-to-noise ratios given typical photo resolutions (e.g., Barnhart et al., 2019; Howell et al., 2020; Zhou et al., 2016). Post-event aerial photos have been supplemented with inferred pre-earthquake topography to reduce noise and measure displacements (Lajoie et al., 2020). Andreuttiova et al. (2022) used legacy aerial photos to measure 3D surface displacements for a large (M_w 7.0 mainshock) event by combining two techniques: optical image correlation for horizontal displacements and subtracting pre- and post-earthquake DSMs for vertical displacements.

3. Methods

This study uses legacy aerial photographs to create SfM-based pre- and post-earthquake DSMs and orthophoto mosaics of the Rangitāiki Plains, as well as a differenced DSM representing coseismic displacement from the Edgecumbe earthquake. These datasets provided the means to map surface rupture, measure coseismic vertical separation, and estimate near-fault horizontal displacement. Other differencing methods were trialed and are discussed below. Our results are then compared to post-earthquake field surveys and measurements from lidar data collected in 2011. We combined our remote measurements with fault information generated in the last few decades to solve for the best-fitting elastic dislocation model of the 1987 Edgecumbe earthquake. Finally, we test whether inflation on a nearby magmatic sill could have promoted slip on faults involved in the Edgecumbe earthquake.

3.1. Aerial Images

We generated SfM-based point clouds using historical photosets from 1972 to 1975 and March 1987 to build pre- and post-earthquake DSMs, respectively (see Open Data for access). Both photosets were scanned using a photogrammetric scanner into digital files at 1800 dpi. The post-earthquake photoset (survey SN8732) consists of 762 images taken with a 152 mm lens on a Zeiss RMK camera at an altitude of ~5,000 feet (~1,524 m). These photos were collected within 1 month of the 2 March Edgecumbe mainshock over four flight dates. The original printed photos are 23 cm square format, scanned to ~18,000 × 16,900 pixels and have footprints ~2.6 km on one edge (extent in Figure S1). This post-earthquake aerial survey was purpose-collected for studying the 1987 Edgecumbe earthquake and is therefore flown at lower altitudes and with greater overlap between adjacent photos than similar New Zealand surveys of this era.

The pre-earthquake photo set (survey SN3580) is composed of 611 images taken with a 210 mm lens on an AT119 Wild RC8 camera at an altitude of ~17,500 feet (~5,334 m) (extent in Figure S1). The entire photoset represents nine flight dates across different seasons and three calendar years, which leads to additional noise and uncertainty in generating the final point cloud and DSM (elaborated on below). The original printed photos were 18 cm square format and scanned to approximately 14,500 × 13,500 pixels, and have footprints ~4.5 km on one edge.

Only one photoset was collected immediately after the earthquake (survey SN8732), but several photo set options exist for the pre-earthquake model. We chose survey SN3580 because although some collection aspects are not ideal (e.g., long collection time window) it had the highest likelihood of success due to a spatial extent larger than the onshore Whakatāne graben (Figure S1), single camera and lens used throughout the entire survey, smaller camera focal length, and lowest flight altitude compared to other photosets. Minimizing time between the pre- and post-earthquake imagery is another important consideration to reduce non-tectonic changes to the landscape; other photosets taken more recently than survey SN3580 (i.e., between 1974 and 1987) likely capture fewer non-tectonic and anthropogenic surface changes. These other photosets, however, lack the resolution required to generate a DSM with sub-meter vertical resolution due to higher flight altitudes, suboptimal camera specifications, poor photo overlap, and limited spatial extent.

3.2. Pre- and Post-Earthquake DSM Generation

The SfM-derived products (e.g., dense point clouds, DSMs, and orthophoto mosaics) were generated using Agisoft Metashape Pro v1.7. We included camera calibration information such as photo fiducial locations and precise camera focal length for both sets of historical photos to improve photo alignment. Other distortion parameters listed in the calibration file were effectively zero at the scale of the photo scan and including these in the SfM process had no noticeable effect on the final DSM.

Some studies suggest that using down-sampled, reduced resolution scanned images (50% original resolution) may improve initial photo alignment by distributing tie points more evenly (Lu et al., 2021). We found that reducing photo resolution here, while keeping other parameters the same, produced poorer results compared to the full resolution scans. This may be a product of the relatively low relief landscape of the Rangitāiki Plains, differences in photogrammetric software, or high degree of anthropogenic modification between collection times. For our data set, we found that increasing the number of key points and tie points above the default values (to 60,000 and 10,000, respectively) substantially improved the initial photo alignment.

Both pre- and post-earthquake photo sets were georeferenced using geographic control point (GCP) coordinates derived from the 2011 lidar point clouds (see Open Data for lidar availability). We placed GCPs on long-standing cultural markers that were visible and unchanged between the pre-and post-earthquake photos and 2011 lidar survey orthoimages. These landmarks are typically bridges (e.g., at the intersection of a concrete deck and the centerline), unique road intersections, statue bases, or property-bounding fence line corners. We avoided GCP sites with irregular surfaces which could introduce elevation uncertainty. The GCP coordinates are derived from the lidar point cloud data rather than the georeferenced orthoimages to reduce uncertainty from image warping. The choice to use lidar-based GCPs is multifold: the lidar data set has the widest extent and is the densest georeferenced data set available remotely for this region; New Zealand Transportation Agency survey benchmarks are not visible in aerial images; the common reference between pre- and post-earthquake photos removes possible long-term changes due to continuous, slow movement (e.g., tectonic plate motions or magma inflation); and the SfM outputs can be easily compared to the more recent lidar topography to identify the largest artifacts and distortions. We use a conservative GCP accuracy of 0.75 and 0.5 m for the pre- and post-earthquake SfM projects, respectively, to account for uncertainty due to photo resolution (~0.35-m-pixel for pre-earthquake; ~0.15-m-pixel for post-earthquake). Unrealistically small accuracy values cause additional warping by forcing the 3D SfM model to pin to potentially inaccurate GCPs, which we noted in early alignment trials.

We placed lidar-based GCPs along the Rangitāiki Plains margin, in the surrounding hills, or in regions with no recorded deformation (i.e., Edgecumbe footwall) to minimize the influence of tectonic and other landscape changes between the photo and lidar surveys (Blick & Flaherty, 1989). This means that control in the interior of the graben, where subsidence was widespread, is sparse, and implies that the resulting models may include absolute spatial inaccuracies.

We found that including "check points" (an Agisoft-software-specific term) during the alignment steps improved the photo alignment and reduced some artifacts. Check points are manually placed markers that link common pixels between photos during photo alignment; they reduce distortion but do not influence georeferencing. Check points improved the pre-earthquake SfM alignment where harsher vignetting (photo darkening away from the center), larger time gaps between photos, less photo overlap, and poorer flight and camera specifications caused sharp, artificial topographic steps between flight lines. In total, we placed 21 control points and 95 check points in the pre-earthquake model and 29 control points and zero check points in the post-earthquake model (Tables S1 and S2).

The final outputs from the pre- and post-earthquake SfM-based point clouds include 2-m DSMs and orthorectified photomosaics (orthophoto mosaics). We subtracted the pre-earthquake DSM from the post-earthquake DSM to produce a 2-m differenced DSM, which was the primary data used to map coseismic deformation (Figure 2a; see Data Repository).

3.3. Fault Mapping

We identified surface ruptures from the 1987 Edgecumbe earthquake using the 2-m differenced DSM (Figure 2; additional files in Data Repository). Mapped fault traces mark relatively linear, continuous (>100-m-long), and discrete changes in vertical difference values. We investigated but ultimately ignored apparent scarps that had persistent trends of exactly north-south or east-west because these result from seams between individual photos and flight lines. Each mapped scarp was checked against the pre- and post-earthquake photomosaics to identify if changes in cultural features or development, such as agricultural plots, could produce an artificial scarp. Scarps with distinct, sharp vertical difference value changes that clearly cross-cut otherwise continuous landforms were mapped as "certain" fault traces. Where the vertical change location was less sharp and displacement occurred over a broader area, we mapped the scarp as an "approximate" fault trace. If the displacement was very broadly distributed, very subtle, or difficult to distinguish, we mapped fault traces as "possible" (examples in Figure 2).

3.4. Measuring Vertical Offsets Across Faults

We extracted swath profiles across the fault scarps from the differenced DSM to measure 1987 coseismic vertical separations. The initial 2-m differenced DSM was resampled to a 4-m grid size using a bilinear interpolation to reduce some of the high-frequency noise originating from the pre-earthquake DSM.

Fault profiles are located on certain or approximate fault traces ~250 m apart, adjusting site locations to avoid non-tectonic topographic changes adjacent to the fault (e.g., vegetation growth, Figures 2c and 2d) and omitting sites with no measureable vertical separation (Figure 3a). Each swath profile was 1-km-long, 30-m-wide, and centered on and orthogonal to the fault scarp (Figure 3) (for description of the profile tool, see Howell, 2021). We selected points on the up- and down-thrown sides of the fault, omitting points from hedgerows, ditches, differential vegetation growth or removal (relative to the other side of the fault), roads, or buildings. We used these points to project lines fit to the hanging wall and footwall to the scarp midpoint distance (Figure 3). The final vertical separation value is the vertical distance between the two projected lines, at the scarp midpoint. The fault location within the scarp has a negligible impact (up to 3 cm) on the final vertical separation measurement because the adjacent surfaces have similar and near-zero slopes. The near-horizontal and planar surfaces in the Rangitāiki Plains mean that vertical separation approximates throw.

To estimate vertical separation uncertainty, we detrended the measurements on each side of the fault by the line of best fit through them and calculate the standard deviation of these detrended points. Our stated 1σ uncertainty in vertical separation is the root mean square (RMS) of the resulting two detrended standard deviations (one on each side of the fault). Other studies have used standard error for displacement profiles (e.g., Zinke et al., 2019) but here, standard error results in very low values (~0.05 m compared to ~0.5 m for standard deviation) due to the good linear fit and the large number of points used. Since the vertical DSM includes scatter up to 1 m vertically along the profile distance (Figure 3), we consider our method to be more conservative and appropriate in this case. The above fault profile methods were repeated using the 2011 lidar 2-m DEM to compare to the differenced DSM measurements and 1987 field-based measurements.

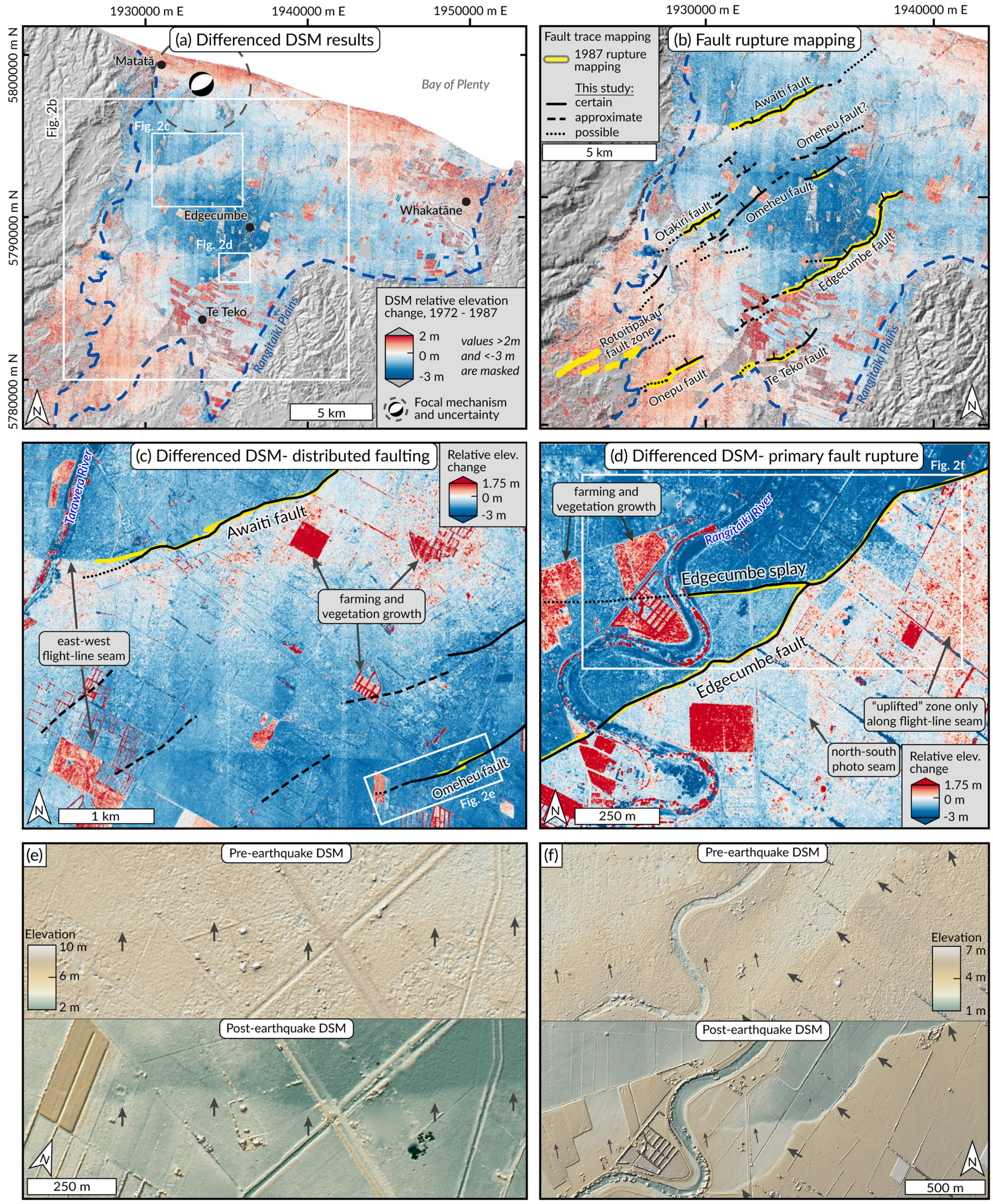
(a) Differenced DSM results
1930000 m E
1940000 m E
1950000 m E
5800000 m N
5790000 m N
5780000 m N
Matatā
Bay of Plenty
Fig. 2b
Fig. 2c
Edgecumbe
Whakatane
Fig. 2d
Te Teko
Rangitaiki Plains
DSM relative elevation change, 1972 - 1987
2 m
0 m
-3 m
values >2m and <-3 m are masked
Focal mechanism and uncertainty
5 km
(b) Fault rupture mapping
Fault trace mapping
1987 rupture mapping
This study:
certain
approximate
possible
5 km
Awaiti fault
Omeheu fault?
Omeheu fault
Otakiri fault
Edgecumbe fault
Rotoitipakau fault zone
Onepu fault
Te Teko fault
(c) Differenced DSM- distributed faulting
Relative elev. change
1.75 m
0 m
-3 m
Tarawera River
Awaiti fault
farming and vegetation growth
east-west flight-line seam
Omeheu fault
Fig. 2e
1 km
(d) Differenced DSM- primary fault rupture
Fig. 2f
farming and vegetation growth
Rangitaiki River
Edgecumbe splay
Edgecumbe fault
"uplifted" zone only along flight-line seam
north-south photo seam
Relative elev. change
1.75 m
0 m
-3 m
250 m
(e)
Pre-earthquake DSM
Elevation
10 m
6 m
2 m
Post-earthquake DSM
250 m
(f)
Pre-earthquake DSM
Elevation
7 m
4 m
1 m
Post-earthquake DSM
500 m

Figure 2.

Finally, to compare all measurement methods and changes in displacement along fault strike, we projected vertical separations from the differenced DSM, lidar DEM, and 1987 field measurements to a central line that parallels the fault zone trend (azimuth 60°/240°) (projection line in Figure 3a).

3.5. Horizontal Displacements and Coseismic Heave

The differenced DSM captures much of the coseismic displacement but does not account for either the strike-slip component or heave. To estimate total coseismic slip, we attempted 3D point cloud differencing using the ICP algorithm (e.g., Nissen et al., 2012; Scott et al., 2019; Wedmore et al., 2019), 2D optical image correlation of the SfM-based orthophoto mosaics (e.g., Leprince et al., 2007), and manual feature matching between pre- and post-earthquake orthophoto mosaics.

The 3D point cloud differencing (e.g., as in Howell et al., 2020) achieved poor results due to relatively flat topography, sparse and small surface features (e.g., buildings and ditches), and high degree of non-tectonic surface change (e.g., farm/crop modification). Similar problems were encountered with the 2D image correlation, with additional problems caused by different shadows from varying sun angles. Finally, we manually measured horizontal movement by drawing the displacement vector between fixed cultural features (e.g., livestock water troughs) on the pre- and post-earthquake orthophoto mosaics. This method was effective, but the resulting horizontal vectors are more sparsely distributed than continuous 3D point cloud or 2D image correlation methods. Additionally, they do not represent absolute displacements because we lack independent pre-earthquake geographic control data. Relative horizontal movements over fairly short distances (<4 km), such as between the hanging wall and footwall of a fault, should be more accurate.

To estimate fault heave along the surface trace, we calculated the coseismic horizontal motion of the hanging wall relative to a fixed footwall. First, we grouped horizontal displacement vectors (within ∼1 km of each other) in the hanging wall and footwall (Figure S2). Each vector group was averaged into a single mean vector. Then, each footwall average vector was subtracted from the corresponding hanging wall average vector to yield the average coseismic horizontal displacement of the hanging wall, relative to the footwall (Table S3). The resulting vectors along the central Edgecumbe fault are oriented ∼90° to the fault trace. Thus, we assume pure normal motion, consistent with field observations (Beanland et al., 1989; Crook & Hannah, 1988), and assume that all horizontal motion is equivalent to heave.

3.6. Elastic Dislocation Model and Coulomb Stress Change Methods

We performed a finite-fault slip inversion to estimate the fault location, geometry, and slip required to produce 1987 surface deformation. The inversion fits a filtered and smoothed differenced DSM. We first removed large vegetation and non-tectonic artifacts by omitting DSM values >0.8 and <−3 m, with additional trimming above −0.5 in the immediate Edgecumbe fault hanging wall. This filtered DSM was then downsampled to a 100 m grid, smoothed by taking the median of displacements within a square 100 m-wide window and trimmed to the central Rangitāiki plains (the primary deformation zone).

We inverted for slip on several fault geometries based on rupture mapping and near-surface dip (from this study; details in subsequent sections), seismic survey data, earthquake waveform, and seismogenic crustal thickness data from the literature. Although some studies invert for fault geometry together with slip distribution (e.g., Scott et al., 2019; Wang et al., 2018), we prefer to specify fault geometry prior to inversion due to our noisy data and lack of horizontal displacement measurements. The interpretations of seismic and gravity surveys suggest that the Edgecumbe fault dips steeply (∼60°) in the upper 1–2 km of the crust (Mouslopoulou et al., 2008). This

Figure 2. Results of structure-from-motion (SfM)-based topographic differencing and coseismic fault trace mapping. Coordinate system in NZGD 2000. (a) Differenced digital surface model (DSM) created by subtracting pre- and post-earthquake SfM-based DSMs, overlain by a hillshade. The relative elevation changes capture shorter-scale displacements along discrete faults and broader patterns of subsidence, but include some artifacts. Extreme difference values (>2 m and <−3 m) are masked to reduce vegetation growth and other noise. Focal mechanism/epicenter from Anderson and Webb (1989). (b) Edgecumbe earthquake surface rupture mapping from this study compared to the trace mapping performed in 1987 by Beanland et al. (1989). All faults except the Rotoitipakau fault zone were identified in this study, and many small fault traces not identified in the field were visible in the differenced DSM. Color scale same as (a). (c) Example of distributed fault mapping and some SfM artifacts. (d) Example of primary fault rupture mapping and some SfM artifacts. (e) Comparison of pre- and post-earthquake topography and subtle fault traces missed during 1987 reconnaissance. Rupture was only mapped along infrastructure (canals) in 1987 but is extended in this study. (f) Pre- and post-earthquake DSMs highlight pre-existing scarps along the primary Edgecumbe fault, but not the splay.

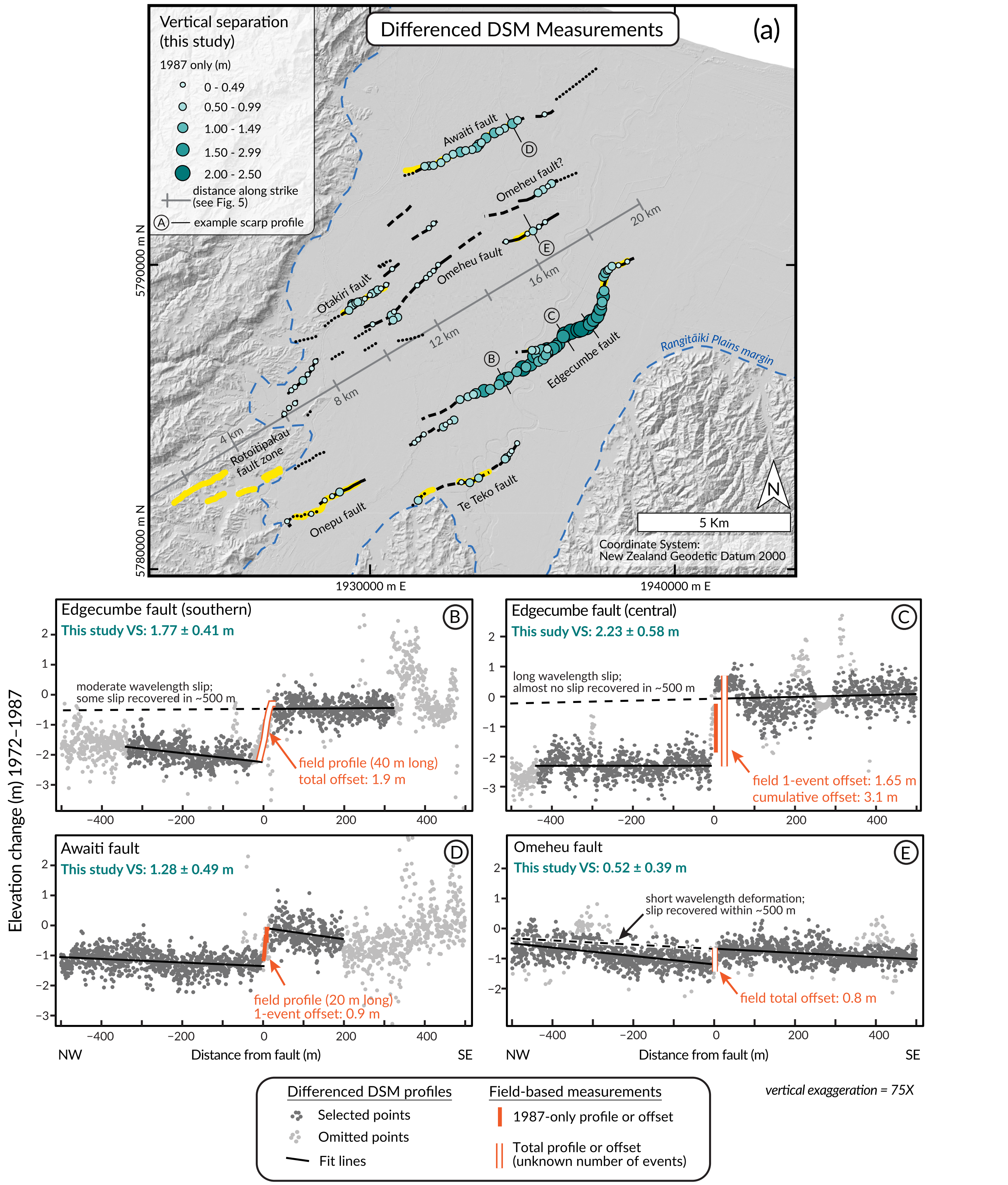

Figure 3. Map view results of differenced digital surface model (DSM) vertical separation measurements and example profiles. (a) Vertical separation measurements (this study) in map view. Beanland et al. (1989) comparison in Figure S6. Along-strike line (gray) used in Figures 4b–4e Examples of profiles across the differenced DSM profiles and comparisons with 1987 field measurements/profiles at the same locations. The longer profile extent from this study (1-km-long compared to <50 m) captures the full vertical separation and changes in displacement wavelength between scarps. Our measurements also capture single event vertical separations rather than cumulative (or unknown event number) displacements measured in 1987.

depth coincides with the depth of alluvial cover above more coherent Matihana ignimbrite and greywacke basement rock (Mouslopoulou et al., 2008) which could influence a change in fault dip as the plane approaches the surface and refracts in differing material (Bray et al., 1994). Deeper fault dips are constrained by 1987 mainshock focal mechanism location and dips, of either 32 + 5/–10° (Webb & Anderson, 1998) or 45 ± 10° (Anderson & Webb, 1989). We prefer the lower dip angle of Webb and Anderson (1998) because it is based on more data, including S-wave seismograms that were absent from the earlier analysis of Anderson and Webb (1989). The seismogenic crust in the Whakatāne graben is approximately 6–8 km thick, which limits the maximum fault depth (Bryan et al., 1999; Robinson, 1989; Taylor et al., 2004). The resulting moment magnitude must fall between 6.4 and 6.6 (Anderson & Webb, 1989; Webb & Anderson, 1998).

We calculated residuals by subtracting the modeled surface displacement from the smoothed differenced DSM values. Initial inversion results produced significant residuals across large areas where little-to-no deformation was observed in 1987 (e.g., in the distal Edgecumbe fault footwall) (Blick & Flaherty, 1989). These residuals are likely caused by poor elevation control in the pre-earthquake model. We therefore applied a global shift to the smoothed DSM before additional inversions to maintain consistency with minimal footwall and far-field surface displacement. The global shift amount (+0.6 m) represents the average value of a 1,500 m × 800 m patch of the smoothed DSM located in the footwall between flight-lines.

The modeled Edgecumbe and Awaiti faults are split into 0.5-km-square tiles with surface displacements calculated using the method of Okada (1985) assuming Lamé parameters μ and ν to be 3×10^{10} Pa and 0.25, respectively. Our slip inversions use the pygmo (Biscani & Izzo, 2020) and NLopt (http://github.com/stevengj/nlopt) libraries, and the monotonic basin hopping and SLSQP algorithms (Kraft, 1988; Wales & Doye, 1997). We use L2-norm minimization and apply Tikhonov Laplacian regularization for each fault by following the L-curve method to choose the best Laplacian weight (Figure S3; e.g., Harris & Segall, 1987). We also penalize slip on all the edges of our modeled fault planes except the up-dip edges, to allow surface rupture.

The best-fit fault geometry is also used to test if stress changes from magmatic sill inflation at depth could promote slip on faults involved in the Edgecumbe earthquake or foreshocks, similar to findings from the Matatā sequence by Hamling et al. (2016) (Figure 1b). We lack focal mechanism or hypocenter data for the foreshock cluster events, but model the foreshock swarm as a southwest-striking, 45° northwest-dipping plane similar to other offshore central Whakatāne graben faults (Lamarche et al., 2006). We test a range of plausible sill locations and extents within the uncertainties from Hamling et al. (2016). Sill inflation was fixed to 1 m, which represents an inflation rate of 20 mm/yr over 50 years (Hamling et al., 2016). Coulomb stress changes were calculated in Coulomb v3.3, assuming a pure normal slip (rake of −90°) (Toda et al., 2011).

4. Differenced DSM, Fault Mapping, and Displacement Results

The SfM processing resulted in pre- and post-event DSMs with resolutions of 68.4 and 30.7 cm grid size, respectively, and orthophoto mosaics of 34.2 and 15.3 cm pixels, respectively (https://doi.org/10.5281/zenodo.7058629). The 2-m DSMs were more useful for mapping because down-sampling reduced high-frequency noise from model artifacts.

We measured displacements along fault traces with about 0.3 m or more of vertical separation along discrete faults (Figure 4). In some instances, fault traces with ≤0.3 m vertical separations were mapped but we could not make accurate measurements within the differenced DSM due to noise that exceeded displacements. An important caveat is that this method, at the resolution of these photos, cannot distinguish shallow buried faulting (i.e., "blind") from discrete surface rupture. Therefore, we refer to any localized tectonic surface deformation along mapped fault traces as surface rupture, though some may be fold scarps.

We mapped a cumulative ~50 km of certain, approximate, and possible fault traces that ruptured in the 1987 Edgecumbe earthquake (Figure 2b). These traces were named based on existing fault mapping (Begg & Mouslopoulou, 2010), but new traces of the Omeheu and Otakiri faults were named based on dip direction (Figure 2b). All fault traces that were mapped in 1987 were mapped here except the Rotoitipakau fault zone (Figure 2b). Additionally, ~32 km of fault traces mapped in this study were not identified in 1987, though these are typically lower confidence and low-amplitude scarps. By comparing the pre-earthquake images and DSM to the differenced DSM, we observed that all mapped fault zones that ruptured in 1987 (Edgecumbe, Awaiti, Te Teko, Omeheu, Otakiri, and Onepu faults) had sections with pre-existing scarps.

10.1029/2022JB024059

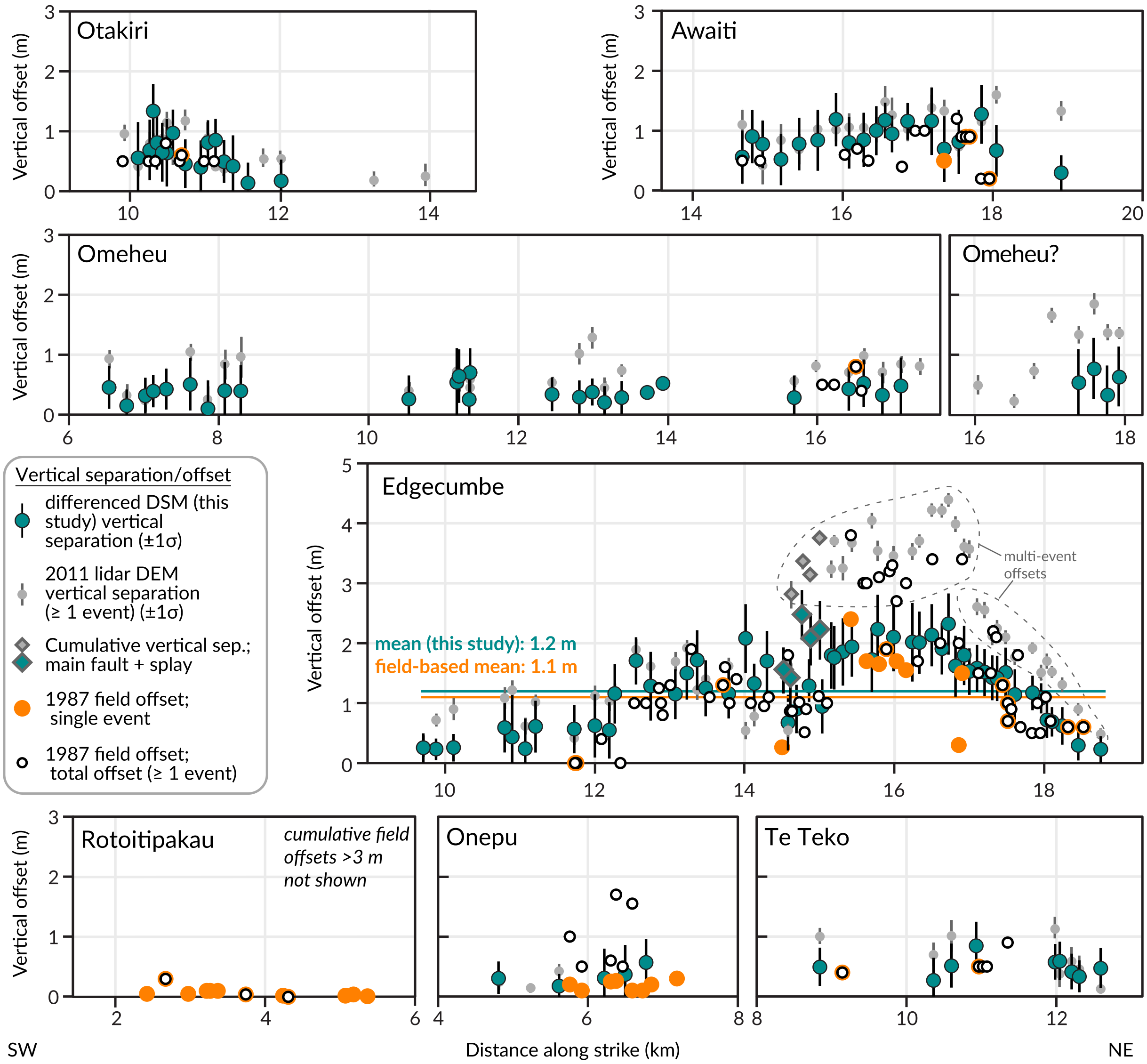

Figure 4. Vertical separations and offset. along fault segments from the structure-from-motion-based differenced digital surface model (DSM) (this study), 1987 field-based measurements (Beanland et al., 1989), and 2011 lidar DEM measurements (this study). Uncertainties from field measurements were not reported. All values are projected to the strike line (see Figure 3). Our differenced DSM measurements typically agree well with and are denser than the field measurements, and are sometimes larger due to longer profiles capturing full deformation (see Figure 3). The differenced DSM is unable to resolve very small displacements (e.g., the Rotoitipakau fault). Lidar-based measurements (gray symbols) confirm that the differenced DSM measurements capture only single-event displacement, compared to the 1987 total offsets (white circles) which may be single or multi-event. Large field-measured pre-existing scarps (>3 m high) from the Rotoitipakau fault not shown here.

Coseismic vertical displacements were measured at 132 fault scarp sites (Figures 3 and 4). The maximum measured vertical separation is 2.5 ± 0.4 m, which combines slip on the main Edgecumbe fault and the small splay near the fault center (Figure 4). The lower limit of measured vertical separations (~0.25–0.3 m) have one standard deviation that is as large as or larger than the vertical separation, which is expected due to the high noise of the pre-earthquake DSM.

The scarp profiles also inform the surface displacement wavelength due to slip on individual fault strands. For example, subsidence in the Edgecumbe and Awaiti fault hanging walls is not fully recovered over 500 m, but slip on the other traces, such as the Omeheu and Otakiri faults, is typically recovered within 200–500 m away from the fault (Figure 3). This wavelength has implications for the fault geometry and slip distribution, and is discussed below (Sections 7 and 8.2).

Horizontal displacement vectors adjacent to the central Edgecumbe fault yielded 21 relative displacements on the hanging wall and 17 relative displacements on the footwall (Figure S2). The hanging wall and footwall groups produced average coseismic heave values of 0.9, 1.0, and 0.7 m (Table S3). The combined throw, heave, and normal rake values yield surface fault dips of 64°, 64°, and 65° (Table S3).

5. Sources of Difference Model Error and Implications for Measurements

The post-earthquake photoset generated a minimally distorted DSM due to the ideal camera lens, short-duration survey, ample photo overlap, and low flight altitude. The pre-earthquake photoset and resulting DSM is lower resolution (68-cm pixels vs. 31-cm pixels) and contains more artifacts; therefore, the pre-event SfM model is a larger source of distortion in the differenced DSM (e.g., Figures 2e and 2f; Figure S4). Distortion occurs primarily in four areas: the coastline, between flight lines, along photoset edges, and in densely vegetated areas. Minor artifacts are also present between individual photos along the seams (e.g., Figure 2d). These distortions manifest as topographic breaks that are aligned due east-west or north-south (parallel to photograph orientations and flight paths) or as long wavelength undulations and doming, and are most apparent when comparing the DSMs (pre- and post-earthquake) to the lidar DEM (Figure S4).

Artifacts around the DSM edges are caused mostly by doming (down-warping away from the photo set center) and dense tree cover (Figure S4). Doming is a known problem common to photogrammetry (e.g., Zhou et al., 2016) and is typically mitigated with additional control points. However here, the areas outside the Rangitāiki plains are heavily forested and repeatedly clear-cut. Dense vegetation typically poorly aligns in Agisoft Metashape Pro; here we suspect that the tree canopy and associated shadows provide few opportunities for unique model tie points used in photo alignment. Forest removal between photo sets also reduces available stable control point locations. Luckily for this study, our focus area is near the photo set center, which is less densely forested and where doming is less problematic.

Previous post-earthquake leveling surveys identified that much of the coast and Rangitāiki Plains either subsided or slightly uplifted during the earthquake, or experienced fluctuations due to groundwater withdrawal or magmatic uplift over longer periods (Figure S5, Table S4) (Blick & Flaherty, 1989; Hamling et al., 2016). Therefore, most of the aerial photos in the Rangitāiki Plains and along the coastline do not contain reliable control point options and likely contain more photo-alignment warping (global shift inaccuracies) than other locations.

Finally, flight line artifacts (east-west striping) (e.g., Figure 2c) were partially reduced, but not eliminated, by including non-georeferenced check points within Agisoft (see Methods). The striping is not homogenous over the field area due to variable photo overlap, photo vignetting, and the multi-year pre-earthquake photo collection duration. Since this striping does not significantly affect the primary results and corrections would require significant and spatially heterogeneous post-processing, we chose not to correct for flight lines.

The artifacts and inaccuracies in these pre- and post-earthquake DSMs have several implications for the resulting differenced DSM. First, long wavelength vertical warping exists over the many-kilometer-scale (~5 km). While some long-wavelength tectonic deformation likely occurred (e.g., Blick & Flaherty, 1989), we cannot necessarily separate these tectonic signals from SfM artifacts. Second, apparent elevation changes across flight lines, or less prominently, across adjacent photos, must be avoided when measuring coseismic vertical separation. Finally, the relatively widely spaced geographic control, long wavelength warping, and more discrete artifacts mean that the difference values at any given point (from the differenced DSM) are likely not representative of absolute coseismic vertical change. This is apparent when comparing field-leveling data to the differenced DSM (Figure S5). For example, large swaths of land southwest of Te Teko did not apparently move in the Edgecumbe earthquake or experienced minor subsidence (Blick & Flaherty, 1989), but appear to have uniformly uplifted in the differenced DSM (Figure 2; Figure S5, Table S4). We therefore consider relative elevation changes across short distances (<2 km), such as taken in fault profiles (Figure 3), to be reliable measures of coseismic deformation. Wider scale deformation patterns are useful to consider in a general sense but may reflect coseismic deformation less reliably.

10.1029/2022JB024059

6. Comparing Displacement Measurements With Field Observations

In order to understand the strengths, weaknesses, and limitations of this technique, it is important to compare the results of SfM-based spatial data to other data collected with established techniques such as field surveys and lidar-based measurements. The 1987 field displacement measurements fell into two categories: single event vertical offsets from the 1987 earthquake and total scarp vertical offsets (Beanland et al., 1989) (Figures 3b and 4; Figure S6, Table S5). The term "offset" is used in the field-based studies and we keep that terminology here—these on-fault measurements may not capture full vertical separation. In some locations, where a reliable displaced marker was present, both single event and total vertical offset were measured (Beanland et al., 1989). In the absence of pre-earthquake topography information, total vertical offsets may represent either 1987-only or multi-event displacements. Beanland et al. (1989) identified pre-existing scarps where a both single event and a larger total scarp height were measured at the same place.

Our coseismic vertical separation measurements generally agree with the field-based measurements (both 1987 single event and total offsets) along the flanks of the Edgecumbe fault and the Otakiri, Awaiti, Omeheu, Onepu, and Te Teko faults (e.g., Figure 3 profile A; Figure 4). An implication of this agreement is that the majority of the total offset field measurements likely only represent 1987 coseismic displacement. Many of our vertical separation values elsewhere are slightly larger than the field estimates when measured in the same location (Figure 4), likely due to the longer profile length and ability to capture the full extent of vertical separation (Figure 4).

Field-based studies identified three faults that re-ruptured in 1987: the central Edgecumbe fault, the Onepu fault, and the Rotoitipakau fault zone (Figure 2). We identified pre-existing scarps on the central Edgecumbe, Onepu, Te Teko, Omeheu, and sections of the Otakiri faults based on the pre-earthquake DSM, expanding the record of multi-event scarps (see Data Repository). We could not identify the small (~10-cm-high) coseismic displacements on the Rotoitipakau fault zone, but lineaments and pre-existing scarps along these fault traces are clearly visible in the pre-earthquake DSM topography, as identified by the field investigations (Beanland et al., 1989). On the central Edgecumbe fault, our vertical separation measurements are similar to field-based single-event offsets and significantly smaller (~0.9–1.3 m smaller) than a cluster of large (>2 m) total offsets and lidar measurements (15.3–17.4 km on Figure 4). This agrees well with previous pre-existing scarp height estimates (1 m from Beanland et al. (1989)) and indicates that the differenced DSM is capturing only coseismic slip rather than cumulative scarp height.

We estimated average heave values of 0.7, 0.9, and 1.0 m near the central Edgecumbe fault, which is broadly consistent with field-based extensional measurements of 0.4–1.6 in the same region. Beanland et al. (1989) estimated a near-surface fault dip of 55°, which is less than our estimated value of ~65°. Our slightly larger single event vertical separation values, which capture the full deformation width across the scarp, likely cause the slightly steeper dip (Figures 3 and 4).

Beanland et al. (1989) calculated an average vertical offset along the Edgecumbe fault of 1.4 m. However, this value simply averages both 1987-only and total offset measurements and does not consider variation in measurement density along the rupture length, which may favor larger, more easily identified offset sites. To try to address these two issues, and to compare to results from this study, we recalculated the average field-based vertical offset by subsampling the likely 1987 offsets.

Our vertical offset/separation mean uses regularly-spaced, 1-km-wide moving-window averages taken every 200 m along the strike distance. Vertical separation values are inversely weighted by the σ^2 value; field measurements are weighted equally because error values were not reported. The final mean displacement value for the Edgecumbe fault is the average of all moving window means for each data set. The recalculated 1987 measurements comprise total vertical and 1987 vertical offsets but excludes offsets >2.5 m (likely multi-event) or clusters identified elsewhere as pre-existing scarp height (e.g., 15.3–17.4 km on Figure 4) (Table S5). The average vertical displacement along the Edgecumbe fault is 1.2 m for field offsets and 1.5 m for differenced DSM vertical separations over the field-measured fault length. Using the SfM-measured fault length, which is ~2.5 km longer (Figure 2b), field vertical offsets average 1.1 m and differenced DSM vertical separations average 1.2 m (Figure 4).

The average vertical displacement values above differ from the 0.6 m reported by Wesnousky (2008), which was incorporated into a global catalog to evaluate potential relationships between earthquake characteristics (e.g.,

10.1029/2022JB024059

Table 1
Elastic Dislocation Fault Parameters and Results

Fault name	Strike (°)	Depth ranges (km)	Dips (°)	Fault length with slip (km)	Rake (°)	Maximum slip (m)
Edgecumbe	237	0–1	65	9.5	270/–90 (normal)	5.80
		1–2	50			
		2–6	35			
Awaiti	244	0–1	65	5.5	270/–90 (normal)	4.79
		1–2	50			
		2–4	45			

Note. Best-fitting fault geometry parameters and results for the Edgecumbe and Awaiti fault from elastic dislocation modeling. Maximum slip is the result of the slip inversion and is sensitive to the degree of smoothing (Table S6); other parameters are based on mapping and displacement data from this study and existing seismological data. Location of faults and slip distributions shown in Figure 5.

length, slip, fault width, moment release). Wesnousky (2008) calculated average displacement by interpolating all offsets from Beanland et al. (1989) along the entire surface rupture length (15.5 km), rather than just the Edgecumbe fault trace. We avoided that approach here because the apparently shallow slip depths associated with the secondary faults may not be appropriate or comparable across a global earthquake catalog (elaborated on in Section 7).

7. Elastic Dislocation Modeling Results and Implications

7.1. Slip Inversion Results

Our new mapping, displacement, and heave and throw results provided additional constraints for a revised elastic dislocation model of the 1987 Edgecumbe earthquake (Table 1). These include a rake of 270/–90 (pure normal), 65° surface dip, fault trace mapping, and a simplified vertical deformation map. Preliminary testing suggested the short wavelength deformation observed across shorter faults is produced by slip at depths <500 m (e.g., Figure 2e). Therefore, we only included the Edgecumbe and Awaiti faults in the slip inversion. All trials used a 10.5-km-long Edgecumbe fault (237° strike) and a 6.5-km-long Awaiti fault (244° strike) based on trace mapping and the imposed slip taper. The modeled Edgecumbe fault extends to 8 km depth, based on seismogenic crust thickness (6–8 km) and centroid depth (6 ± 1 km) (Beanland et al., 1990; Bryan et al., 1999; Robinson, 1989; Taylor et al., 2004; Webb & Anderson, 1998). The modeled Awaiti fault has a maximum depth of 4 km, based on the shorter rupture and narrower deformation extent. Although a trade-off between slip on the Edgecumbe and Awaiti faults could conceivably affect our results, we did not observe one. We attribute this lack of trade-off to the 8-km separation between the faults and the concentration of slip on the Awaiti fault at shallow depths.

We first tested a simple planar Edgecumbe and Awaiti geometry with 65° dips and a multi-part fault with steep surface and 45° dips at depth (Figures S8 and S9). These are broadly consistent with simple estimates of the overall TVZ (Villamor & Berryman, 2001) and Whakatāne graben fault dips in the New Zealand Community Fault Model (Seebeck et al., 2022). However, the disagreement between relatively low-angle focal mechanism dips (32° + 5/–10°) (Webb & Anderson, 1998) and near-surface dips (~65°; this study) suggests the Edgecumbe fault dip is steeper near the surface and gentler at depth. Additionally, the approximate centroid location, which is 9 ± 3 km away from the Edgecumbe fault trace and about 6 ± 1 km deep (Webb & Anderson, 1998), implies an overall fault dip ≤45°.

We find that the regional displacement field is best approximated with an Edgecumbe fault that dips 65° from 0 to 1 km, 50° from 1 to 2 km, and 35° from 2 to 8 km depths (Figure 5a; Table 1). The modeled Awaiti fault dips 65° from 0 to 1 km, 50° from 1 to 2 km, and 45° from 2 to 4 km depths. On the Edgecumbe fault, slip reaches a maximum of 5.80 m, is centered down-dip of the peak surface slip at mid-range seismogenic depths (~4 km) and, and tapers to zero toward the lateral and bottom fault edges (Figure 5b). This fault geometry and slip yields an earthquake with M_w 6.5, which agrees with M_w 6.5 of Webb and Anderson (1998) and Anderson et al. (1990).

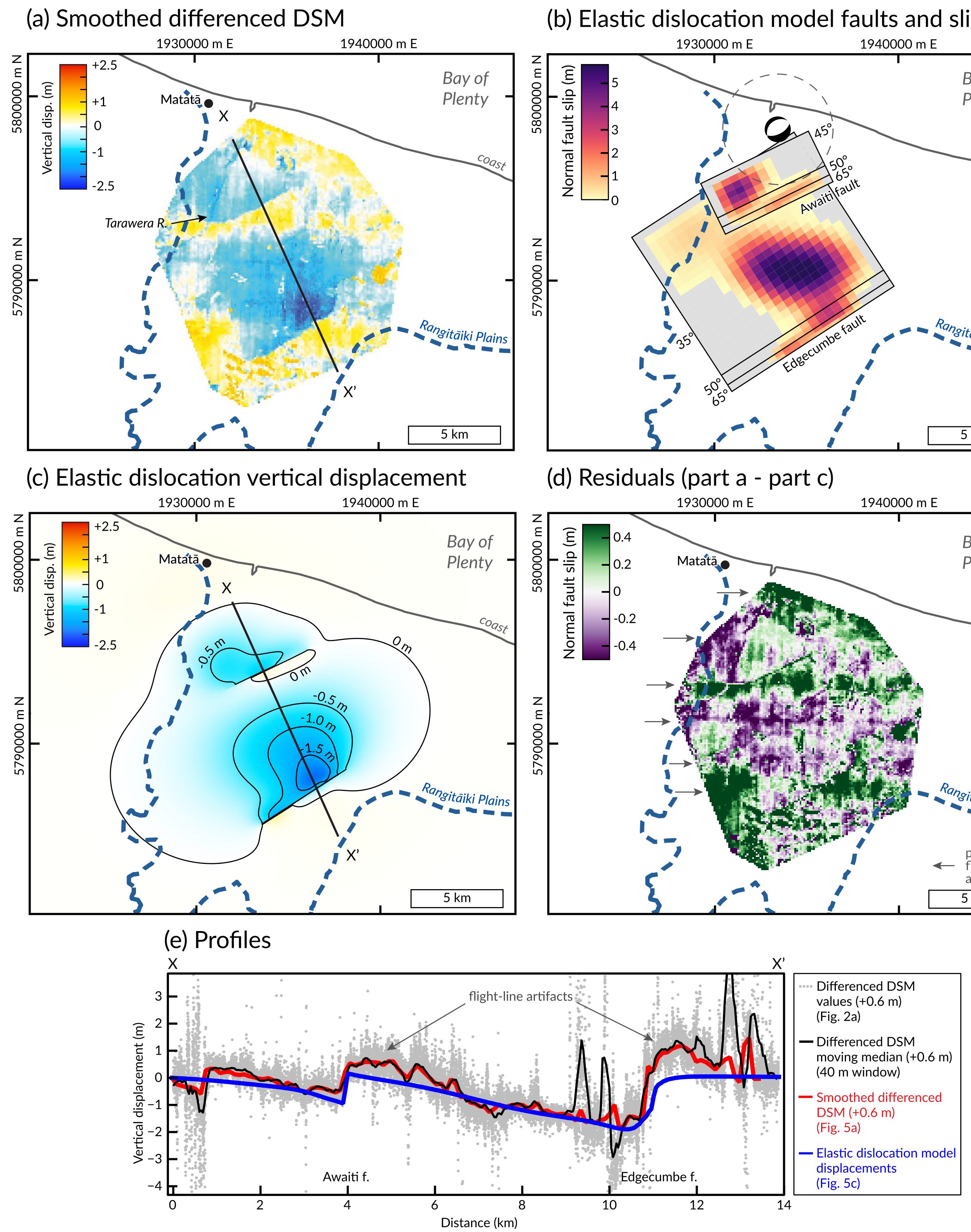

(a) Smoothed differenced DSM
1930000 m E
1940000 m E
5800000 m N
5790000 m N
Vertical disp. (m)
+2.5
+1
0
-1
-2.5
Matatā
X
X'
Bay of Plenty
coast
Tarawera R.
Rangitāiki Plains
5 km
(b) Elastic dislocation model faults and slip
Normal fault slip (m)
5
4
3
2
1
0
45°
50°
65°
Awaiti fault
35°
Edgecumbe fault
(c) Elastic dislocation vertical displacement
0 m
-0.5 m
-1.0 m
-1.5 m
(d) Residuals (part a - part c)
0.4
0.2
-0.2
-0.4
prominent flight line artifacts
(e) Profiles
Vertical displacement (m)
Distance (km)
flight-line artifacts
Awaiti f.
Edgecumbe f.
Differenced DSM values (+0.6 m) (Fig. 2a)
Differenced DSM moving median (+0.6 m) (40 m window)
Smoothed differenced DSM (+0.6 m) (Fig. 5a)
Elastic dislocation model displacements (Fig. 5c)

Figure 5.

Residuals between the elastic dislocation displacements and the differenced DSM are generally <0.25 m, with slightly higher residuals near larger DSM artifacts (e.g., flight lines) (Figure 5d). We note that the degree of smoothing has a relatively small effect on the fit to observed displacements but has a larger effect on maximum slip (Table S6); the RMS misfit of our least smoothed solution is 0.41 m (residual norm of 48.6), compared with 0.44 m (residual norm 52.8) for our most smoothed model. Far-field and small on-fault displacements may be overshadowed by non-tectonic surface changes like compaction or bank failure near rivers, resulting in less accurate slip distributions. Our preferred fault geometry matches field leveling data better than the other trials, with minimal footwall uplift and similar zero-displacement contour locations (Figure S7). The alternative steeper fault geometries, based on published dip values, produce higher residuals and greater footwall uplift compared to the preferred geometry and do not intersect the mainshock centroid location (Figures S8 and S9). Further alternative inversion results are available in the Data Repository (Text S1).

At >2 km depths, our modeled dip value (35°) is similar to the previous planar elastic dislocation model dip estimate (40°), which was informed by relative horizontal displacements from triangulation networks (Darby, 1989). The most significant differences between our slip inversion and the previous model of Darby (1989) are a heterogeneous slip distribution, gentler overall fault dip, dip change with depth, and the addition of the Awaiti fault. The data available for this inversion cannot distinguish listric (i.e., smooth decrease in dip with depth) from multi-part planar fault geometries. In the case of the latter, near-surface dip changes could be due to surface crust failing under tension, consistent with dominantly planar geometry observed in other active normal faults (e.g., Reynolds & Copley, 2018). For the Edgecumbe fault, these geometry differences do not impact on the overall rupture area, moment release, or expected seismic hazard since the seismogenic crust is fairly thin and dip changes likely occur within the upper few kilometers of the crust in either case.

7.2. Implications of a Gentle Dip for the Edgecumbe Fault

Lower angle normal faults do not fit traditional Andersonian theory (Anderson, 1951), but 35° does fall within the observed dip range of 30–60° observed globally on normal faults (Collettini & Sibson, 2001; Jackson, 1987; Middleton & Copley, 2014; Reynolds & Copley, 2018; Wernicke, 1995). The fault hosting the M_w 5.7 2020 Magna earthquake in Utah, USA, was inferred to have a similar geometry to our preferred Edgecumbe fault model; focal mechanisms suggest a gently dipping (20–32°) fault plane at depth that steepens to 70° near the surface, though no surface rupture was observed in that event (Pang et al., 2020). The Edgecumbe earthquake can thus provide an important case study of rupture behavior and surface deformation patterns when gently-dipping normal faults rupture to the surface through the width of the seismogenic crust.

The 1987 Edgecumbe earthquake deformation field can be approximated without the smaller secondary faults. This, along with very short wavelength surface deformation on those secondary structures (e.g., Figure 4e), suggests these faults did not host substantial slip at depth, did not link at depth with other seismogenic faults during this earthquake, and did not contribute significant moment release during the 1987 earthquake. Shallow slip on these faults, however, does not preclude deeper slip in other earthquakes.

Previously inferred dips for TVZ faults (60°), estimated as a compromise between gentler deep and very steep surface dips (Villamor & Berryman, 2001), are steeper than our results. Additionally, the preferred dip on the Edgecumbe fault in the Community Fault Model (a simplified fault network for hazard analyses) is 50° ± 10°, which we consider an unlikely representative dip (Text S1, Figures S8 and S9) (Seebeck et al., 2022). If, like the Edgecumbe fault, other TVZ faults have lower dip angles for the majority of their area, this could influence both slip rate and earthquake size estimates for the region. Alternatively, the Edgecumbe fault may have lower overall dip values than the average Taupō rift fault because it is a primary graben-bounding structure that has rotated farther from an initially steeper dip (e.g., Jackson, 1987). More information about fault dip at depths >1–2 km is needed to improve seismic hazard estimates throughout the Taupō rift.

Figure 5. Comparison of elastic dislocation model slip and deformation to structure-from-motion-based vertical displacement of the 1987 Edgecumbe earthquake. (a) The differenced digital surface model (DSM) was smoothed over a 100-m-moving-median window and trimmed to the interest extent. Most "uplift" is likely an artifact from poor photo overlap between frames and flight lines (see Figure 2) and other problems described in the text. All values have been shifted up by 0.6 m to correct for lack of geographic control within the graben and flight line distortion. (b) Best-fitting slip on the simplified Edgecumbe and Awaiti faults. Dip values labeled per segment row. (c) Vertical surface displacement from the slip shown in (b). (d) Residuals between the smoothed DSM and elastic dislocation vertical displacement. East-west trends in residuals caused by flight line artifacts. (e) Graben profiles comparing differenced DSM values (shifted up 0.6 m) and the elastic dislocation model vertical displacement from (b).

10.1029/2022JB024059

8. Pushing the Limits: Lessons Learned in Reconstructing Moderate Magnitude Earthquake Deformation Fields From Historical Imagery

This study has two main foci: the development of a technique using historical aerial photos to build pre- and post-earthquake spatial data, and the implications of our results for the Edgecumbe area and greater TVZ. We therefore separate our discussion by focusing first on the application of our method and second on the tectonics of the onshore Whakatāne graben.

8.1. Advantages and Limitations of Surface Displacement Measurements From Legacy Aerial Photos

We have shown that using historical aerial photos to generate DSMs can be an effective and useful technique, particularly in the absence of other high-resolution topographic data. Moderate-magnitude events like the 1987 Edgecumbe earthquake are valuable to study because they occur more frequently than larger earthquakes, but the smaller displacements are more challenging to characterize (e.g., Wedmore et al., 2019). The primary advantages of the technique used here include the abilities to (a) take dense measurements and fill in spatial gaps from previous surveys, (b) measure displacements across a wide aperture, including distributed deformation and off-fault displacement, (c) identify subtle deformation that is difficult to recognize on the ground, (d) discern between new fault scarps and pre-existing fault scarps, and (e) estimate the depth of faulting based on surface deformation width.

In this study, we resolved vertical deformation confidently to ∼0.3 m in our differenced DSM (Figure 4). We located nearly all of the fault traces mapped in post-earthquake reconnaissance, and in some cases, mapped traces that were not identified following the earthquake (Figure 2). The newly-mapped 1987 rupture traces are typically extensions of known scarps or wide, low-amplitude (<0.5-m-high) scarps several hundreds of meters from other mapped fault traces. In the absence of surface cracking, discrete breaks from surface rupture, or obviously deformed cultural markers, these scarps would be very difficult or impossible to detect in the field.

The limitations and challenges of this technique depend on the geographic setting and photoset properties, but generally include artifacts from flight lines, long wavelength warping, and limited final product resolution. Factors such as high flight altitude, poor photo overlap (<60%), too short or too long lens focal lengths, presence of clouds or harsh shadows, photo vignetting, and long photo survey duration will all negatively impact the SfM process. In this study, these problems were highlighted by the quality difference between the pre- and post-earthquake DSMs—the post-earthquake photos generated a much clearer, lower-noise, and higher resolution DSM than the pre-earthquake photos (Figure 2; Figure S4). The Rotoitipakau fault zone rupture could not be mapped on the differenced DSM (Figure 2b) due to a combination of artifacts and very small displacements (∼10 cm; Beanland et al., 1989). This suggests that there may be other 1987-activated fault traces with small vertical separations (<30 cm) that remain undocumented by either field or differenced DSM mapping, particularly if brittle deformation at the surface was absent. Precise independent ground control, if available, can reduce some model artifacts, but errors introduced during point cloud generation (e.g., warping between control points) can be difficult to quantify (Delano et al., 2021).

We were unable to accurately resolve the effects of tectonic subsidence from sediment compaction and other non-tectonic processes in this study. Broad-scale sediment compaction in unconsolidated alluvial fill and pore water movement was documented to some extent post-earthquake, but was poorly constrained and likely spatially heterogeneous due to variable sediment deposits and groundwater distribution (Blick & Flaherty, 1989). Where measured, the vertical effects of sediment compaction were ∼0.2–0.3 m (Blick & Flaherty, 1989; Pender & Robertson, 1987), which is generally less than one standard deviation of our displacement measurements. Sediment compaction near the Tarawera and Rangitaiki rivers may have contributed to areas in the elastic dislocation slip distribution with under-fit subsidence (Figures 2c, 2d and 5; Figure S7). Untangling non-tectonic ground deformation at this scale from tectonic displacement is a challenge that extends beyond this study and method. Accurately quantifying non-tectonic processes would require more information on subsurface materials and properties, and some form of control that can be compared before and after the earthquake.

10.1029/2022JB024059

8.2. Role of Minor Faults During Coseismic Deformation

The Edgecumbe earthquake is a moderate magnitude earthquake with short primary fault rupture length (i.e., the Edgecumbe fault) compared to average and maximum slip, a high degree of secondary faulting, and wide faulted zone compared to global catalogs of normal fault earthquakes. For example, normal fault earthquakes have an average-to-maximum surface slip ratio of 0.35 ± 0.11 m, and only 30% of events show distributed faulting at 7 km from the primary fault (Ferrario & Livio, 2021; Wesnousky, 2008); our results show a ratio of 0.48 and distributed faulting at distances up to ∼8 km from the Edgecumbe fault. Fault displacement hazard curves ultimately hinge on data from past events, so improving rupture mapping accuracy directly impacts hazard estimates derived from global catalogs (e.g., Ferrario & Livio, 2018, 2021). Based on our mapping and Rotoitipakau fault traces from Beanland et al. (1989), there was 17.6 km of primary fault (Edgecumbe and Awaiti) surface rupture and 36.8 km of secondary fault surface rupture (Figure 2b). If we consider only the certain and approximate traces, these values are 15.9 km (38%) for primary and 25.9 km (62%) for secondary traces. Most other well-studied historical normal fault ruptures, such as those in the western U.S., produced more localized fault rupture along narrower zones than observed here (e.g., Caskey et al., 1996; DuRoss et al., 2019; Wallace et al., 2004). Therefore, the significant secondary surface rupture may reflect the magmatic-tectonic rift setting where the lithosphere is relatively thin, weak, and hot (Gase et al., 2019). Some conditions thought to control distributed faulting in the M_w 6.5 2016 Central Italy earthquake—a moderate-magnitude normal earthquake with significant secondary faulting—are also present in the Whakatāne graben (i.e., normal fault slip and thick sediment cover) though other characteristics (like position within the graben) differ (Ferrario & Livio, 2018).

Surface deformation on secondary structures, which likely did not have significant slip at depth or contribute to seismic moment, is important from a fault displacement hazard perspective (ANSI/ANS, 2015; Ferrario & Livio, 2018). For example, during the 2016 Kaikōura earthquake, minor surface slip occurred on the Hope fault without apparent slip at depth, causing road damage and suggesting that this phenomenon may be common in New Zealand earthquakes (Litchfield et al., 2018). Multi-fault and distributed surface rupture and associated hazards may be overlooked when only concentrating on metrics such as magnitude, fault length, peak or average slip, or fault zone width. The observation that some faults produced a scarp without deeper slip also has important implications for paleoseismic records, since the earthquake history interpreted from trenches in these settings becomes more complicated. In the case of the Rangitāiki Plains, past interpretation of the number paleoearthquakes assumes primary rupture on most scarps which, which without extensive timing data and information regarding multi-fault rupture behavior, could lead to an overestimation of earthquake frequency (e.g., Begg & Mouslopoulou, 2010).

8.3. Possible Magma-Tectonic Interactions in the Rangitāiki Plains

Understanding the interactions between magmatic and seismic activity is critical to characterize both volcanic and earthquake hazard in active rift settings like the TVZ. The 1987 Edgecumbe earthquake is generally considered an amagmatic earthquake within the tectonically-dominated northern TVZ (Muirhead et al., 2022; Rowland et al., 2010). Hamling et al. (2016), however, demonstrated that an inflating sill at depth along the western margin of the Rangitāiki Plains may control longer term uplift and produce stress changes that promote earthquakes, such as the 2005–2009 Matatā sequence.

One of the Edgecumbe earthquake foreshock clusters occurred in a similar location to (∼10 km farther west) and along trend with the 2005–2009 Matatā sequence (Figure 1b) (Smith & Oppenheimer, 1989). Importantly, the margins of the best fit sill location determined by Hamling et al. (2016) coincide with the approximate hypocenter of the 1987 Edgecumbe earthquake and both foreshock clusters (Figures 1b and 6). The similarity between the Edgecumbe and the Matatā sequences leads to the question: could the Edgecumbe earthquake sequence have been triggered by stress changes from an inflating sill below Matatā?

We explored the idea of magma-inflation-triggered earthquakes within the Whakatāne graben by modeling the sill geometry and inflation used in Hamling et al. (2016) and imposing the resulting static stress on simplified versions of the Edgecumbe fault, Awaiti fault, and approximate planar fit to the eastern 1987 foreshock cluster (Figure 6). Depending on the location and depth of the sill, the imposed sill inflation causes static stress changes that either promote or inhibit slip on portions of the simplified faults. In general, positive stress changes occur with two sill configurations. When the sill and lower fault edges are at similar depths, and the sill is northwest of

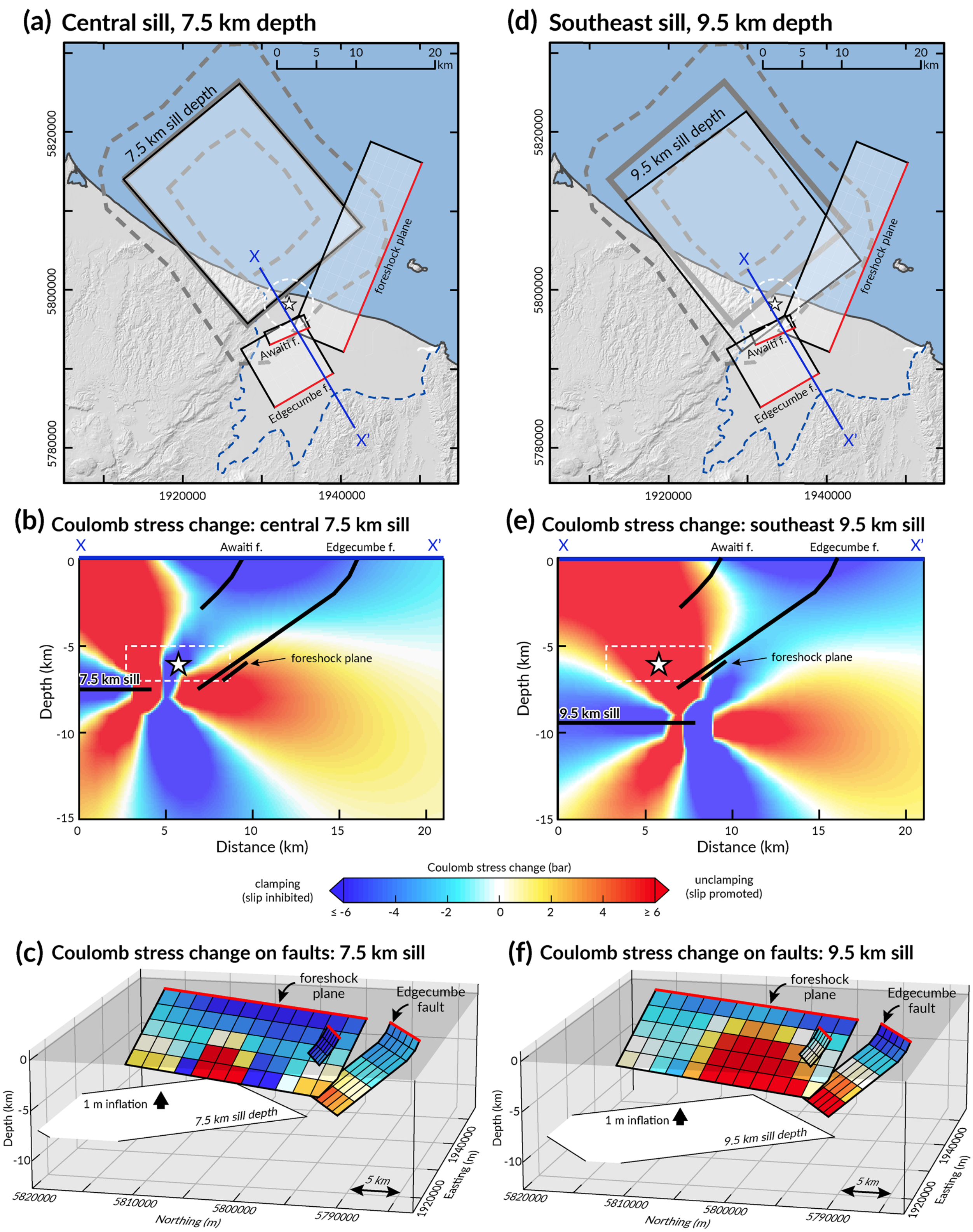
(a) Central sill, 7.5 km depth
(d) Southeast sill, 9.5 km depth
7.5 km sill depth
9.5 km sill depth
foreshock plane
Awaiti f.
Edgecumbe f.
X
X'
(b) Coulomb stress change: central 7.5 km sill
(e) Coulomb stress change: southeast 9.5 km sill
Depth (km)
Distance (km)
7.5 km sill
9.5 km sill
Coulomb stress change (bar)
clamping
(slip inhibited)
unclamping
(slip promoted)
(c) Coulomb stress change on faults: 7.5 km sill
(f) Coulomb stress change on faults: 9.5 km sill
foreshock plane
Edgecumbe fault
1 m inflation
Northing (m)
Easting (m)
5 km

Figure 6.

the faults, slip is promoted on the lower Edgecumbe and foreshock faults (Figures 6a–6c). When the sill edge ends below the modeled faults at any depth, slip is promoted on all three faults (Edgecumbe, foreshock, and Awaiti planes) at deeper depths (Figures 6d–6f).

The existence of reasonable sill inflation models that promote slip on these faults suggests a plausible scenario where as the sill inflates, slip is triggered at depth on favorably oriented nearby faults, as was inferred in the Matatā sequence by Hamling et al. (2016). Further, slip at greater depths on either the Edgecumbe or foreshock plane faults results in positive static stress changes that promote slip in both along-strike and up-dip directions. Mouslopoulou et al. (2008) inferred that the moderately asymmetric cumulative throw and 1987 slip distribution, as well as south-directed rupture propagation in 1987, might be caused by changes in stress controlled by the intersection of the northern Edgecumbe fault with the Waiohau fault (Figure 1). We confirm this asymmetry at the surface and at depth (Figures 4 and 5) and further speculate that the hypocenter location and asymmetric slip distribution could at least in part be caused by enhanced stress due to sill inflation. While further work would be required to confirm a stress triggering mechanism for this particular earthquake, the cumulative displacement asymmetry (Mouslopoulou et al., 2008) is consistent with observations that faults may preferentially grow laterally away from magma bodies (Dumont et al., 2017) and that the location of maximum slip typically occurs on the more structurally mature sections of the faults (Perrin et al., 2016).

The TVZ contains active faults above the underlying magmatic bodies and many mechanisms have been proposed for volcano-tectonic interactions and triggering (Figure 1) (Muirhead et al., 2022; Rowland et al., 2010; Villamor & Berryman, 2001; Wilson & Rowland, 2016). Though generally considered tectonically driven, it is possible that the timing of the 1987 Edgecumbe earthquake may have been advanced by the interaction with long-term sill inflation and increased stress on adjacent faults.

9. Conclusions

We have demonstrated that historical aerial photos can be used to construct SfM-based pre- and post-earthquake topographic models useful for detecting coseismic surface deformation. When applied to the M_w 6.5 1987 Edgecumbe earthquake in New Zealand, we find that our measurements generally agree with, but are slightly larger than, field-based measurements. We also detected many more small, subtle scarps than were mapped in the field survey. As a result, our understanding of surface deformation from this earthquake is improved by a denser vertical displacement data set, clearer distinction between the 1987 and pre-existing scarps, and wider aperture displacement field that captures off-fault deformation.

The improved surface displacement data constrain updated fault geometries and a new elastic dislocation model of the earthquake, which compared to earlier efforts, now includes spatially variable slip, gentler fault dips at depth, steep fault dips in the near surface, and the inclusion of the Awaiti fault. The 1987 Edgecumbe earthquake is somewhat unusual in the amount of surface rupture on dominantly secondary (non-seismogenic at depth) faults for a moderate-magnitude event. The prevalence of secondary surface rupture may be a result of the intra-rift setting with associated thick sediment cover and thin seismogenic crust; such behavior should be taken into account in probabilistic surface displacement hazard assessments for this type of structural setting. Finally, we have shown that the Edgecumbe fault could have been pushed to rupture by stress changes associated with an inflating sill at depth. This finding suggests that the timing of moderate-to-large "tectonic" earthquakes may be advanced by fault interaction with magmatic processes like sill inflation and the cascading influence of stress changes on adjacent faults.

Figure 6. Stress changes on Edgecumbe earthquake sequence faults from sill inflation. The best-fit sill location (solid gray rectangle), location uncertainty (thick dashed gray polygons), depths (9.5 km ± 2.1 km), and inflation of 1 m (20 mm/yr over 50 years) from Hamling et al. (2016). The Edgecumbe and Awaiti faults are the same as in Figure 5, but with patches ~2.5 × 2.5 km. The foreshock plane follows the trend of 1987 foreshocks with a 45° dip. Epicenter (star) location and uncertainty (thin white dash) from Anderson and Webb (1989); depth and uncertainty is from Webb and Anderson (1998). (a–c) Location of faults and stress changes for a central sill location at 7.5 km depth. The base of the Edgecumbe and foreshock fault planes are in zones of increased Coulomb stress. (d–f) Location of faults and modeled stress changes for a southeastern sill at 9.5 km depth. Large portions of the base of the Edgecumbe, foreshock, and Awaiti faults occur in zones of increased Coulomb stress. Both configurations are examples where sill inflation promotes slip near the observed 1987 foreshocks and mainshock epicenter and centroid depth. In (b and e), stress changes are relative to a fault with strike/dip/rake of 240/45/-90.

Data Availability Statement

Aerial images used in this study were freely sourced from the LINZ Data Service and licensed by Crown Aerial Film Archive for reuse under the CC BY 3.0 license. Bay of Plenty lidar point clouds available from ftp://files.boprc.govt.nz/Public (accessible using Internet Explorer). The Data Repository includes Text S1, Figures S1–S9, Tables S1–S6, rupture mapping from 1987 and this study, reactivated scarp mapping, displacement shapefiles, pre- and post-earthquake DSMs and orthomosaics, and the differenced DSM (https://doi.org/10.5281/zenodo.7058629).

Acknowledgments

We thank reviewers Chelsea Scott and Luke Wedmore and Editor Isabelle Manighetti for their contributions to improving the manuscript. Useful early discussion with David Napier, Graeme Blick, Pilar Villamor, Kelvin Berryman, Jonathan Davidson, Ed Nissen, Lia Lajoie, and Andy Nicol helped guide the foundations of this research. Narges Khajavi provided preliminary fault trace mapping and digitized pre-existing mapping. This research was funded by the University of Canterbury Mason Trust, QuakeCoRE, and the New Zealand Earthquake Commission (EQC). Partial support was provided by the New Zealand Ministry of Business, Innovation and Employment (MBIE) through the Hazard Risk Management program (Strategic Science Investment Fund, contract C05X1702). Open access publishing facilitated by University of Canterbury, as part of the Wiley - University of Canterbury agreement via the Council of Australian University Librarians.

References

Abdullah, Q., Bethel, J., Hussain, M., & Munjy, R. (2013). Photogrammetric project and mission planning. *Manual of Photogrammetry* (pp. 1187–1220). American Society for Photogrammetry and Remote Sensing.

Ambraseys, N. N. (1963). The Buyin-Zara (Iran) earthquake of September, 1962 a field report. *Bulletin of the Seismological Society of America*, *53*(4), 705–740. https://doi.org/10.1785/bssa0530040705

Anderson, E. M. (1951). *The dynamics of faulting and dike formation with application to Britain* (2nd ed.). Oliver and Boyd.

Anderson, H., Smith, E., & Robinson, R. (1990). Normal faulting in a back arc basin: Seismological characteristics of the March 2, 1987, Edgecumbe, New Zealand, Earthquake. *Journal of Geophysical Research*, *95*(B4), 4709. https://doi.org/10.1029/JB095iB04p04709

Anderson, H., & Webb, T. (1989). The rupture process of the 1987 Edgecumbe earthquake, New Zealand. *New Zealand Journal of Geology and Geophysics*, *32*(1), 43–52. https://doi.org/10.1080/00288306.1989.10421387

Andreuttiova, L., Hollingsworth, J., Vermeesch, P., Mitchell, T. M., & Bergman, E. (2022). Revisiting the 1959 Hebgen Lake earthquake using optical image correlation; new constraints on near-field 3D ground displacement. *Geophysical Research Letters*, *49*(16), e2022GL098666. https://doi.org/10.1029/2022GL098666

ANSI/ANS. (2015). *ANSI/ANS-2.30: Criteria for assessing tectonic surface fault rupture and deformation at nuclear facilities*. American Nuclear Society.

Ayoub, F., Leprince, S., & Avouac, J. (2009). Co-registration and correlation of aerial photographs for ground deformation measurements. *ISPRS Journal of Photogrammetry and Remote Sensing*, *64*(6), 551–560. https://doi.org/10.1016/j.isprsjprs.2009.03.005

Bakker, M., & Lane, S. N. (2017). Archival photogrammetric analysis of river–floodplain systems using Structure from Motion (SfM) methods. *Earth Surface Processes and Landforms*, *42*(8), 1274–1286. https://doi.org/10.1002/esp.4085

Barnhart, W. D., Gold, R. D., & Hollingsworth, J. (2020). Localized fault-zone dilatancy and surface inelasticity of the 2019 Ridgecrest earthquakes. *Nature Geoscience*, *13*(10), 699–704. https://doi.org/10.1038/s41561-020-0628-8

Barnhart, W. D., Gold, R. D., Shea, H. N., Peterson, K. E., Briggs, R. W., & Harbor, D. J. (2019). Vertical coseismic offsets derived from high-resolution stereogrammetric DSM differencing: The 2013 Baluchistan, Pakistan earthquake. *Journal of Geophysical Research*, *17*, 6039–6055.

Beanland, S., Berryman, K. R., & Blick, G. H. (1989). Geological investigations of the 1987 Edgecumbe earthquake, New Zealand. *New Zealand Journal of Geology and Geophysics*, *32*(1), 73–91. https://doi.org/10.1080/00288306.1989.10421390

Beanland, S., Blick, G. H., & Darby, D. J. (1990). Normal faulting in a back arc basin: Geological and geodetic characteristics of the 1987 Edgecumbe Earthquake, New Zealand. *Journal of Geophysical Research*, *95*(B4), 4693–4707. https://doi.org/10.1029/JB095iB04p04693

Begg, J. G., & Mouslopoulou, V. (2010). Analysis of late Holocene faulting within an active rift using lidar, Taupo Rift, New Zealand. *Journal of Volcanology and Geothermal Research*, *190*(1–2), 152–167. https://doi.org/10.1016/j.jvolgeores.2009.06.001

Bemis, S. P., Micklethwaite, S., Turner, D., James, M. R., Akciz, S., Thiele, S. T., & Bangash, H. A. (2014). Ground-based and UAV-based photogrammetry: A multi-scale, high-resolution mapping tool for structural geology and paleoseismology. *Journal of Structural Geology*, *69*, 163–178. https://doi.org/10.1016/j.jsg.2014.10.007

Biscani, F., & Izzo, D. (2020). A parallel global multiobjective framework for optimization: Pagmo. *Journal of Open Source Software*, *5*(53), 2338. https://doi.org/10.21105/joss.02338

Blick, G. H., & Flaherty, M. P. (1989). Regional vertical deformation associated with the 1987 Edgecumbe earthquake, New Zealand. *New Zealand Journal of Geology and Geophysics*, *32*(1), 99–108. https://doi.org/10.1080/00288306.1989.10421392

Bray, J. D., Seed, R. B., Cluff, L. S., & Seed, H. B. (1994). Earthquake fault rupture propagation through soil. *Journal of Geotechnical Engineering*, *120*(3), 543–561. https://doi.org/10.1061/(ASCE)0733-9410(1994)120:3(543)

Bryan, C. J., Sherburn, S., Bibby, H. M., Bannister, S. C., & Hurst, A. W. (1999). Shallow seismicity of the central Taupo Volcanic Zone, New Zealand: Its distribution and nature. *New Zealand Journal of Geology and Geophysics*, *42*(4), 533–542. https://doi.org/10.1080/00288306.1999.9514859

Caskey, S. J., Wesnousky, S. G., Zhang, P., & Slemmons, D. B. (1996). Surface faulting of the 1954 fairview peak (MS 7.2) and dixie valley (MS 6.8) earthquakes, central Nevada. *Bulletin of the Seismological Society of America*, *86*(3), 761–787. https://doi.org/10.1785/BSSA0860030761

Collettini, C., & Sibson, R. H. (2001). Normal faults, normal friction? *Geology*, *29*(10), 927–930. https://doi.org/10.1130/0091-7613(2001)029<0927:NFNF>2.0.CO;2

Crook, C. N., & Hannah, J. (1988). Regional horizontal deformation associated with the March 2, 1987, Edgecumbe earthquake, New Zealand. *Geophysical Research Letters*, *15*(4), 361–364. https://doi.org/10.1029/GL015i004p00361

Darby, D. J. (1989). Dislocation modelling of the 1987 Edgecumbe earthquake, New Zealand. *New Zealand Journal of Geology and Geophysics*, *32*(1), 115–122. https://doi.org/10.1080/00288306.1989.10421394

Delano, J. E., Briggs, R. W., DuRoss, C. B., & Gold, R. D. (2021). Quick and dirty (and accurate) 3D paleoseismic trench models using coded scale bars. *Seismological Research Letters*, *92*(6), 3526–3537. https://doi.org/10.1785/0220200246

Derrien, A., Villeneuve, N., Peltier, A., & Beauducel, F. (2015). Retrieving 65 years of volcano summit deformation from multitemporal structure from motion: The case of Piton de la Fournaise (La Réunion Island). *Geophysical Research Letters*, *42*(17), 6959–6966. https://doi.org/10.1002/2015GL064820

Duffy, B., Quigley, M., Barrell, D. J. A., Van Dissen, R., Stahl, T., Leprince, S., et al. (2013). Fault kinematics and surface deformation across a releasing bend during the 2010 MW 7.1 Darfield, New Zealand, earthquake revealed by differential LiDAR and cadastral surveying. *The Geological Society of America Bulletin*, *125*(3–4), 420–431. https://doi.org/10.1130/B30753.1

Dumont, S., Klinger, Y., Socquet, A., Doubre, C., & Jacques, E. (2017). Magma influence on propagation of normal faults: Evidence from cumulative slip profiles along Dabbahu-Manda-Hararo rift segment (Afar, Ethiopia). *Journal of Structural Geology*, *95*, 48–59. https://doi.org/10.1016/j.jsg.2016.12.008

DuRoss, C. B., Bunds, M. P., Gold, R. D., Briggs, R. W., Reitman, N. G., Personius, S. F., & Toké, N. A. (2019). Variable normal-fault rupture behavior, northern Lost River fault zone, Idaho, USA. *Geosphere*, *15*(6), 1–24. https://doi.org/10.1130/GES02096.1

Ekhtari, N., & Glennie, C. (2018). High-resolution mapping of near-field deformation with airborne Earth observation data, a comparison study. *IEEE Transactions on Geoscience and Remote Sensing*, *56*(3), 1598–1614. https://doi.org/10.1109/TGRS.2017.2765601

Elliott, J. R., Walters, R. J., & Wright, T. J. (2016). The role of space-based observation in understanding and responding to active tectonics and earthquakes. *Nature Communications*, *7*(1), 13844. https://doi.org/10.1038/ncomms13844

Ferrario, M. F., & Livio, F. (2018). Characterizing the distributed faulting during the 30 October 2016, central Italy earthquake: A reference for fault displacement hazard assessment. *Tectonics*, *37*(5), 1256–1273. https://doi.org/10.1029/2017TC004935

Ferrario, M. F., & Livio, F. (2021). Conditional probability of distributed surface rupturing during normal-faulting earthquakes. *Solid Earth*, *12*(5), 1197–1209. https://doi.org/10.5194/se-12-1197-2021

Gase, A. C., Van Avendonk, H. J. A., Bangs, N. L., Luckie, T. s. W., Barker, D. H. N., Henrys, S. A., et al. (2019). Seismic evidence of magmatic rifting in the offshore Taupo Volcanic Zone, New Zealand. *Geophysical Research Letters*, *46*(22), 12949–12957. https://doi.org/10.1029/2019GL085269

Gomez, C., Hayakawa, Y., & Obanawa, H. (2015). A study of Japanese landscapes using structure from motion derived DSMs and DEMs based on historical aerial photographs: New opportunities for vegetation monitoring and diachronic geomorphology. *Geomorphology*, *242*, 11–20. https://doi.org/10.1016/j.geomorph.2015.02.021

Hamling, I. J., Hreinsdóttir, S., Bannister, S., & Palmer, N. (2016). Off-axis magmatism along a subaerial back-arc rift: Observations from the Taupo Volcanic Zone, New Zealand. *Science Advances*, *2*(6), e1600288. https://doi.org/10.1126/sciadv.1600288

Harris, R. A., & Segall, P. (1987). Detection of a locked zone at depth on the Parkfield, California, segment of the San Andreas fault. *Journal of Geophysical Research*, *92*(B8), 7945. https://doi.org/10.1029/JB092iB08p07945

Henderson, J. (1933). Geological aspects of the Hawkes Bay earthquakes. *New Zealand Journal of Science and Technology*, *15*, 38–75.

Howell, A. (2021). Fault profile tool (v0.1) [Computer software]. Zenodo. Retrieved from https://zenodo.org/record/5525497%23.Y2SfYXZBxPY

Howell, A., Nissen, E., Stahl, T., Clark, K., Kearse, J., Van Dissen, R., et al. (2020). Three-dimensional surface displacements during the 2016 M_W 7.8 Kaikōura earthquake (New Zealand) from photogrammetry-derived point clouds. *Journal of Geophysical Research: Solid Earth*, *125*(1). https://doi.org/10.1029/2019JB018739

Jackson, J. A. (1987). Active normal faulting and crustal extension. *Geological Society, London, Special Publications*, *28*(1), 3–17. https://doi.org/10.1144/GSL.SP.1987.028.01.02

Kelsey, H. M., Hull, A. G., Cashman, S. M., Berryman, K. R., Cashman, P. H., Trexler, J. H., Jr., & Begg, J. G. (1998). Paleoseismology of an active reverse fault in a forearc setting: The Poukawa fault zone, Hikurangi forearc, New Zealand. *GSA Bulletin*, *110*(9), 1123–1148. https://doi.org/10.1130/0016-7606(1998)110<1123:POAARF>2.3.CO;2

Koehler, R. D., Dee, S., Elliott, A., Hatem, A., Pickering, A., Pierce, I., & Seitz, G. (2021). Field response and surface-rupture characteristics of the 2020 M 6.5 Monte Cristo range earthquake, central walker Lane, Nevada. *Seismological Research Letters*, *92*(2A), 823–839. https://doi.org/10.1785/0220200371

Kraft, D. (1988). A software package for sequential quadratic programming. Forschungsbericht- Deutsche Forschungs-und Versuchsanstalt Fur Luft-und Raumfahrt.

Krauss, K. (1993). *Photogrammetry, volume 1: Fundamentals and standard processes*. Dümmlers Verlag.

Lajoie, L. J., Nissen, E., Johnson, K. L., & Lajoie, K. R. (2020). Submeter resolution surface rupture topography from legacy aerial photographs—A test case from the 1992 landers earthquake. *Earth and Space Science*, *7*(3). https://doi.org/10.1029/2019EA000651

Lamarche, G., Barnes, P. M., & Bull, J. M. (2006). Faulting and extension rate over the last 20, 000 years in the offshore Whakatane Graben, New Zealand continental shelf. *Tectonics*, *25*(4). https://doi.org/10.1029/2005TC001886

Langridge, R. M., Ries, W. F., Litchfield, N. J., Villamor, P., Van Dissen, R. J., Barrell, D., et al. (2016). The New Zealand active faults database. *New Zealand Journal of Geology and Geophysics*, *59*(1), 86–96. https://doi.org/10.1080/00288306.2015.1112818

Leprince, S., Barbot, S., Ayoub, F., & Avouac, J. (2007). Automatic and precise orthorectification, coregistration, and subpixel correlation of satellite images, application to ground deformation measurements. *IEEE Transactions on Geoscience and Remote Sensing*, *45*(6), 1529–1558. https://doi.org/10.1109/tgrs.2006.888937

Litchfield, N. J., Villamor, P., Van Dissen, R. J., Nicol, A., Barnes, P. M., Barrell, D. J. A., et al. (2018). Surface rupture of multiple crustal faults in the 2016 Mw 7.8 Kaikōura, New Zealand, earthquake. *Bulletin of the Seismological Society of America*, *108*(3B), 1496–1520. https://doi.org/10.1785/0120170300

Lu, L., Zhou, Y., & Walker, R. T. (2021). Using historical aerial photographs to measure earthquake deformation: Testing the effects of scan resolution. *Remote Sensing of Environment*, *252*, 112118. https://doi.org/10.1016/j.rse.2020.112118

Manighetti, I., Perrin, C., Dominguez, S., Garambois, S., Gaudemer, Y., Malavieille, J., et al. (2015). Recovering paleoearthquake slip record in a highly dynamic alluvial and tectonic region (Hope Fault, New Zealand) from airborne Lidar. *Journal of Geophysical Research: Solid Earth*, *120*(6), 4484–4509. https://doi.org/10.1002/2014JB011787

Manighetti, I., Perrin, C., Gaudemer, Y., Dominguez, S., Stewart, N., Malavieille, J., & Garambois, S. (2020). Repeated giant earthquakes on the Wairarapa fault, New Zealand, revealed by Lidar-based paleoseismology. *Scientific Reports*, *10*(1), 2124. https://doi.org/10.1038/s41598-020-59229-3

Middleton, T. A., & Copley, A. (2014). Constraining fault friction by re-examining earthquake nodal plane dips. *Geophysical Journal International*, *196*(2), 671–680. https://doi.org/10.1093/gji/ggt427

Middleton, T. A., Walker, R. T., Parsons, B., Lei, Q., Zhou, Y., & Ren, Z. (2016). A major, intraplate, normal-faulting earthquake: The 1739 Yinchuan event in northern China. *Journal of Geophysical Research: Solid Earth*, *121*(1), 293–320. https://doi.org/10.1002/2015JB012355

Midgley, N. G., & Tonkin, T. N. (2017). Reconstruction of former glacier surface topography from archive oblique aerial images. *Geomorphology*, *282*, 18–26. https://doi.org/10.1016/j.geomorph.2017.01.008

Milliner, C., Dolan, J. F., Hollingsworth, J., Leprince, S., Ayoub, F., & Sammis, C. G. (2015). Quantifying near-field and off-fault deformation patterns of the 1992 M w 7.3 landers earthquake: Deformation of the landers earthquake. *Geochemistry, Geophysics, Geosystems*, *16*(5), 1577–1598. https://doi.org/10.1002/2014GC005693

Mouslopoulou, V., Nicol, A., Walsh, J. J., Beetham, D., & Stagpoole, V. (2008). Quaternary temporal stability of a regional strike-slip and rift fault intersection. *Journal of Structural Geology*, *30*(4), 451–463. https://doi.org/10.1016/j.jsg.2007.12.005

Muirhead, J. D., Illsley-Kemp, F., Barker, S. J., Villamor, P., Wilson, C. J. N., Otway, P., et al. (2022). Stretching, shaking, inflating: Volcanic-tectonic interactions at a rifting silicic caldera. *Frontiers of Earth Science*, *10*. https://doi.org/10.3389/feart.2022.835841

Nissen, E., Krishnan, K., Aravindhan, K., Arrowsmith, J. R., & Saripalli, S. (2012). Three-dimensional surface displacements and rotations from differencing pre- and post-earthquake LiDAR point clouds. *Geophysical Research Letters*, *39*(16), L16301. https://doi.org/10.1029/2012GL052460

Nissen, E., Maruyama, T., Ramon Arrowsmith, J., Elliott, J. R., Krishnan, A. K., Oskin, M. E., & Saripalli, S. (2014). Coseismic fault zone deformation revealed with differential Lidar: Examples from Japanese Mw ∼7 intraplate earthquakes. *Earth and Planetary Science Letters*, *405*, 244–256. https://doi.org/10.1016/j.epsl.2014.08.031

Okada, Y. (1985). Surface deformation due to shear and tensile faults in a half-space. *Bulletin of the Seismological Society of America*, *75*(4), 1135–1154. https://doi.org/10.1785/BSSA0750041135

Oskin, M. E., Arrowsmith, J. R., Corona, A. H., Elliott, A. J., Fletcher, J. M., Fielding, E. J., et al. (2012). Near-field deformation from the El Mayor-Cucapah earthquake revealed by differential LIDAR. *Science*, *335*(6069), 702–705. https://doi.org/10.1126/science.1213778

Ota, Y., Beanland, S., Berryman, K. R., & Nairn, I. A. (1988). The Matata fault: Active faulting at the northwestern margin of the whakatane graben, eastern Bay of Plenty. *New Zealand Geological Survey Record*, *35*, 6–13.

Pang, G., Koper, K. D., Mesimeri, M., Pankow, K. L., Baker, B., Farrell, J., et al. (2020). Seismic analysis of the 2020 Magna, Utah, earthquake sequence: Evidence for a listric wasatch fault. *Geophysical Research Letters*, *47*(18), e2020GL089798. https://doi.org/10.1029/2020GL089798

Pender, M. J., & Robertson, T. W. (Eds.). (1987). Edgecumbe earthquake: Reconnaissance report, *Bulletin of the New Zealand national society for earthquake engineering* (Vol. *20*, pp. 201–249). https://doi.org/10.1193/1.1585452

Perrin, C., Manighetti, I., Ampuero, J., Cappa, F., & Gaudemer, Y. (2016). Location of largest earthquake slip and fast rupture controlled by along-strike change in fault structural maturity due to fault growth. *Journal of Geophysical Research: Solid Earth*, *121*(5), 3666–3685. https://doi.org/10.1002/2015JB012671

Reitman, N. G., Bennett, S. E. K., Gold, R. D., Briggs, R. W., & DuRoss, C. B. (2015). High-resolution trench photomosaics from image-based modeling: Workflow and error analysis. *Bulletin of the Seismological Society of America*, *105*(5), 2354–2366. https://doi.org/10.1785/0120150041

Reynolds, K., & Copley, A. (2018). Seismological constraints on the down-dip shape of normal faults. *Geophysical Journal International*, *213*(1), 534–560. https://doi.org/10.1093/gji/ggx432

Robinson, R. (1989). Aftershocks of the 1987 Edgecumbe earthquake, New Zealand: Seismological and structural studies using portable seismographs in the epicentral region. *New Zealand Journal of Geology and Geophysics*, *32*(1), 61–72. https://doi.org/10.1080/00288306.1989.10421389

Rowland, J. V., Wilson, C. J. N., & Gravley, D. M. (2010). Spatial and temporal variations in magma-assisted rifting, Taupo Volcanic Zone, New Zealand. *Journal of Volcanology and Geothermal Research*, *190*(1), 89–108. https://doi.org/10.1016/j.jvolgeores.2009.05.004

Schermer, E. R., Van Dissen, R., Berryman, K. R., Kelsey, H. M., & Cashman, S. M. (2004). Active faults, paleoseismology, and historical fault rupture in northern Wairarapa, North Island, New Zealand. *New Zealand Journal of Geology and Geophysics*, *47*(1), 101–122. https://doi.org/10.1080/00288306.2004.9515040

Scott, C., Arrowsmith, J. R., Nissen, E., Lajoie, L., Maruyama, T., & Chiba, T. (2018). The M7 2016 Kumamoto, Japan, earthquake: 3-D deformation along the fault and within the damage zone constrained from differential lidar topography. *Journal of Geophysical Research: Solid Earth*, *123*(7), 6138–6155. https://doi.org/10.1029/2018JB015581

Scott, C., Bunds, M., Shirzaei, M., & Toke, N. (2020). Creep along the central san andreas fault from surface fractures, topographic differencing, and InSAR. *Journal of Geophysical Research: Solid Earth*, *125*(10), e2020JB019762. https://doi.org/10.1029/2020JB019762

Scott, C., Champenois, J., Klinger, Y., Nissen, E., Maruyama, T., Chiba, T., & Arrowsmith, R. (2019). The 2016 M7 Kumamoto, Japan, earthquake slip field derived from a joint inversion of differential Lidar topography, optical correlation, and InSAR surface displacements. *Geophysical Research Letters*, *46*(12), 6341–6351. https://doi.org/10.1029/2019GL082202

Seebeck, H., Van Dissen, R. J., Litchfield, N. J., Barnes, P. M., Nicol, A., Langridge, R. M., et al. (2022). New Zealand community fault model—version 1.0. https://doi.org/10.21420/GA7S-BS61

Shao, Y., Liu-Zeng, J., Van der Woerd, J., Klinger, Y., Oskin, M. E., Zhang, J., et al. (2020). Late Pleistocene slip rate of the central Haiyuan fault constrained from optically stimulated luminescence, 14C, and cosmogenic isotope dating and high-resolution topography. *GSA Bulletin*, *133*(7–8), 1347–1369. https://doi.org/10.1130/B35571.1

Smith, E. G. C., & Oppenheimer, C. M. M. (1989). The Edgecumbe earthquake sequence: 1987 February 21 to March 18. *New Zealand Journal of Geology and Geophysics*, *32*(1), 31–42. https://doi.org/10.1080/00288306.1989.10421386

Stahl, T. A., Niemi, N. A., Delano, J. E., Wolfe, F. D., Bunds, M. P., & Howell, A. (2021). Diffuse tectonic deformation in the Drum Mountains fault zone, Utah, USA: Testing the utility of legacy aerial photograph-derived topography. *Frontiers of Earth Science*, *8*, 597. https://doi.org/10.3389/feart.2020.600729

Taylor, S. K., Bull, J. M., Lamarche, G., & Barnes, P. M. (2004). Normal fault growth and linkage in the Whakatane Graben, New Zealand, during the last 1.3 Myr. *Journal of Geophysical Research*, *109*(B2), B02408. https://doi.org/10.1029/2003JB002412

Toda, S., Stein, R. S., Sevilgen, V., & Lin, J. (2011). *Coulomb 3.3 Graphic-rich deformation and stress-change software for earthquake, tectonic, and volcano research and teaching—User guide*. U.S. Geological Survey Open-File Report No. (p. 63). Retrieved from http://pubs.usgs.gov/of/2011/1060/

Trexler, C. C., Morelan, A. E., Oskin, M. E., & Kreylos, O. (2018). Surface slip from the 2014 South Napa earthquake measured with structure from motion and 3-D virtual reality. *Geophysical Research Letters*, *45*(12), 5985–5991. https://doi.org/10.1029/2018GL078012

Villamor, P., & Berryman, K. (2001). A late Quaternary extension rate in the Taupo Volcanic Zone, New Zealand, derived from fault slip data. *New Zealand Journal of Geology and Geophysics*, *44*(2), 243–269. https://doi.org/10.1080/00288306.2001.9514937

Wales, D. J., & Doye, J. P. K. (1997). Global optimization by basin-hopping and the lowest energy structures of Lennard-Jones clusters containing up to 110 atoms. *The Journal of Physical Chemistry A*, *101*(28), 5111–5116. https://doi.org/10.1021/jp970984n

Wallace, L. M., Beavan, J., McCaffrey, R., & Darby, D. (2004). Subduction zone coupling and tectonic block rotations in the North Island, New Zealand. *Journal of Geophysical Research*, *109*(B12), B12406. https://doi.org/10.1029/2004JB003241

Wang, T., Wei, S., Shi, X., Qiu, Q., Li, L., Peng, D., et al. (2018). The 2016 Kaikōura earthquake: Simultaneous rupture of the subduction interface and overlying faults. *Earth and Planetary Science Letters*, *482*, 44–51. https://doi.org/10.1016/j.epsl.2017.10.056

Webb, T. H., & Anderson, H. (1998). Focal mechanisms of large earthquakes in the North Island of New Zealand: Slip partitioning at an oblique active margin. *Geophysical Journal International*, *134*(1), 40–86. https://doi.org/10.1046/j.1365-246x.1998.00531.x

Wedmore, L. N. J., Gregory, L. C., McCaffrey, K. J. W., Goodall, H., & Walters, R. J. (2019). Partitioned off-fault deformation in the 2016 Norcia earthquake captured by differential terrestrial laser scanning. *Geophysical Research Letters*, *46*(6), 3199–3205. https://doi.org/10.1029/2018GL080858

Wernicke, B. (1995). Low-angle normal faults and seismicity: A review. *Journal of Geophysical Research*, *100*(B10), 20159–20174. https://doi.org/10.1029/95JB01911

10.1029/2022JB024059

Wesnousky, S. G. (2008). Displacement and geometrical characteristics of earthquake surface ruptures: Issues and implications for seismic-hazard analysis and the process of earthquake rupture. *Bulletin of the Seismological Society of America*, *98*(4), 1609–1632. https://doi.org/10.1785/0120070111

Westoby, M. J., Brasington, J., Glasser, N. F., Hambrey, M. J., & Reynolds, J. M. (2012). "Structure-from-Motion" photogrammetry: A low-cost, effective tool for geoscience applications. *Geomorphology*, *179*, 300–314. https://doi.org/10.1016/j.geomorph.2012.08.021

Wilson, C. J. N., Houghton, B. F., McWilliams, M. O., Lanphere, M. A., Weaver, S. D., & Briggs, R. M. (1995). Volcanic and structural evolution of Taupo volcanic zone, New Zealand: A review. *Journal of Volcanology and Geothermal Research*, *68*(1), 1–28. https://doi.org/10.1016/0377-0273(95)00006-G

Wilson, C. J. N., & Rowland, J. V. (2016). The volcanic, magmatic and tectonic setting of the Taupo Volcanic Zone, New Zealand, reviewed from a geothermal perspective. *Geothermics*, *59*, 168–187. https://doi.org/10.1016/j.geothermics.2015.06.013

Yagi, Y., Okuwaki, R., Enescu, B., Kasahara, A., Miyakawa, A., & Otsubo, M. (2016). Rupture process of the 2016 Kumamoto earthquake in relation to the thermal structure around Aso volcano. *Earth Planets and Space*, *68*(1), 118. https://doi.org/10.1186/s40623-016-0492-3

Youngs, R. R., Arabasz, W. J., Anderson, R. E., Ramelli, A. R., Ake, J. P., Slemmons, D. B., et al. (2003). A methodology for probabilistic fault displacement hazard analysis (PFDHA). *Earthquake Spectra*, *19*(1), 191–219. https://doi.org/10.1193/1.1542891

Zhou, Y., Walker, R. T., Hollingsworth, J., Talebian, M., Song, X., & Parsons, B. (2016). Coseismic and postseismic displacements from the 1978 M w 7.3 Tabas-e-Golshan earthquake in eastern Iran. *Earth and Planetary Science Letters*, *452*, 185–196. https://doi.org/10.1016/j.epsl.2016.07.038

Zinke, R., Hollingsworth, J., Dolan, J. F., & Van Dissen, R. (2019). Three-dimensional surface deformation in the 2016 M W 7.8 Kaikōura, New Zealand, earthquake from optical image correlation: Implications for strain localization and long-term evolution of the Pacific-Australian plate boundary. *Geochemistry, Geophysics, Geosystems*, *20*(3), 1609–1628. https://doi.org/10.1029/2018GC007951